LOW CONVECTIVE FIELD ARTIFACT ELIMINATION USING DIELECTRIC PADDING AND MULTICHANNEL RECEIVE IN CR-MREPT CONDUCTIVITY IMAGES

A THESIS SUBMITTED TO

THE GRADUATE SCHOOL OF ENGINEERING AND SCIENCE

OF BILKENT UNIVERSITY

IN PARTIAL FULFILLMENT OF THE REQUIREMENTS FOR

THE DEGREE OF

MASTER OF SCIENCE

IN

ELECTRICAL AND ELECTRONICS ENGINEERING

By

Gülşah Yıldız

August 2018

LOW CONVECTIVE FIELD ARTIFACT ELIMINATION USING DIELECTRIC PADDING AND MULTICHANNEL RECEIVE IN CR-MREPT CONDUCTIVITY IMAGES

By Gülşah Yıldız

August 2018

We certify that we have read this thesis and that in our opinion it is fully adequate, in scope and in quality, as a thesis for the degree of Master of Science.

Yusuf Ziya İder(Advisor)

Ergin Atalar

Nevzat Güneri Gençer

Approved for the Graduate School of Engineering and Science:

Ezhan Karaşan
Director of the Graduate School

ABSTRACT

LOW CONVECTIVE FIELD ARTIFACT ELIMINATION USING DIELECTRIC PADDING AND MULTICHANNEL RECEIVE IN CR-MREPT CONDUCTIVITY IMAGES

Gülşah Yıldız
M.S. in Electrical and Electronics Engineering
Advisor: Yusuf Ziya İder
August 2018

Imaging the electrical conductivity of the tissues in RF frequencies is an important tool for medical diagnostic purposes along with the local specific absorption rate estimation that is closely related to MR safety aspects. Magnetic Resonance Electrical Properties Tomography (MREPT) algorithms use the fact that the electrical properties of the object of interest perturb the B_1 field and that they can be reconstructed by solving an inverse problem that requires the measured B_1 field. Convection-reaction-equation based magnetic resonance electrical properties tomography (cr-MREPT) provides conductivity images that are boundary artifact free and robust against noise in contrast to conventional MREPT algorithms. However, these images suffer from the Low Convective Field (LCF) artifact. This thesis propose two methods to eliminate the LCF artifact. One of which is to use dielectric pads in alternating positions to modify the transmit magnetic field and shift the LCF region from each other in different excitation data. Within an electromagnetic model, pads with different parameters (electrical properties, pad thickness, pad height, arc angle, and thickness of the pad-object gap) are simulated. First, the effect of high dielectric and high conductive pads onto the B_1 field is analyzed. Then, two data sets with the pad located on various locations of the object (phantom) are acquired, and the corresponding linear system of equations are simultaneously solved (combined) to get LCF artifact free conductivity images. In experimental studies, water pads and $BaTiO_3$ pads are used with agar-saline phantoms. In general, a pad should have 180° arc angle and the same height with the phantom for maximum benefit. Also, the closer the pad is to the phantom, the more pronounced is its effect. Increasing the pad thickness and/or the relative permittivity of the pad increases the LCF shift while excessive amounts of these parameters cause errors

in conductivity reconstructions because of the failure in the assumption made such that the z-component of the magnetic field (H_Z) is neglected in the solution. Conductivity of the pad, on the other hand, has minimal effect on elimination of the LCF artifact. Using the proposed technique, LCF artifact is removed and also the reconstructed conductivity values are improved. Thick water pads are proved to be better than the thin ones whereas high dielectric pads must be preferred as thin. The drawbacks of this method are that the acquisition time increases with the multiples of the excitation number and that the H_Z assumption may fail to validate significantly with the choice of pad parameters. The second method proposes a solution that requires 1 excitation only and circumvents the LCF artifact. It uses the difference between the receive sensitivities of a multichannel receive coil as a means to alter the LCF regions in each channel data. Although it loses its accuracy for a non-quadrature coil, transceive phase assumption, which approximates the transmit phase as the half of the transcieve phase, is utilized and the data formed from different channels are combined to reconstruct LCF-free conductivity images. Comparing the results, this latter technique is superior to the original method as LCF artifact is eliminated and is superior to the padding technique as it requires at least half the time required for padding. However, the multichannel receive method lacks accuracy due to the incorrect phase, whereas it can be a valuable tool for non-quantitative conductivity imaging that only the contrast between the neighboring tissues is sufficient.

Keywords: Magnetic Resonance Electrical Properties Tomography (MREPT), convection reaction equation based MREPT (cr-MREPT), electrical property imaging, conductivity imaging, Padding, LCF, multichannel electrical property imaging.

ÖZET

DİELEKTRİK YASTIK VE ÇOK KANALLI ALICI KULLANIMI İLE KR-MREÖT İLETKENLİK GÖRÜNTÜLERİNDE DÜŞÜK KONVEKTİF BÖLGE ARTEFAKTLARININ GİDERİMİ

Gülşah Yıldız
Elektrik Elektronik Mühendisliği, Yüksek Lisans
Tez Danışmanı: Yusuf Ziya İder
Ağustos 2018

RF frekanslarında dokuların elektrik iletkenliğini görüntülemek, MR güvenliği ile yakından ilişkili lokal özgül soğurma hızı kestirimi ile birlikte tıbbi teşhis açısından önemli bir araçtır. Manyetik Rezonans Elektriksel Özellikler Tomografisi (MREÖT) algoritmaları, ilgilenilen nesnenin elektriksel özelliklerinin B1 alanı nda birtakı m bozulmalar yarattığını ve B1 alanı ölçümlerini kullanan bir ters problem çözülerek yeniden yapılandırılabileceği fikrini kullanır. Konveksiyon-reaksiyon denklemi tabanlı Manyetik Rezonans Elektriksel Özellikler Tomografisi (kr-MREÖT), geleneksel MREÖT algoritmaları nı n aksine, sı nır artefaktı olmayan ve gürültüye karşı dayanıklı iletkenlik görüntüleri sağlar. Buna karşın, bu görüntüler Düşük Konvektif Bölge (DKB) artefaktından muzdariptir. Bu tezde, DKB artefaktını ortadan kaldırmak için iki yöntem önerilmektedir. Birinci yöntemde, dielektrik yastıklar, verici manyetik alanını değiştirmek ve DKB bölgesini, farklı uyarımlarda birbirine göre kaydırmak için değişik pozisyonlarda kullanılır. Bir elektromanyetik modelde farklı parametrelere sahip yastıklar (elektriksel özellikler, yastık kalınlığı, yastık yüksekliği, yay açısı ve yastık-nesne boşluğunun kalınlığı) benzetimi elde edildi. İlk olarak, yüksek dielektrik ve yüksek iletken yastıkların B1 alanına etkisi analiz edildi. Daha sonra, fantomun etrafında çeşitli pozisyonlara yerleştirilen yastık ile iki veri seti elde edilir ve DKB artefaktı olmayan iletkenlik görüntüleri elde etmek için, söz konusu doğrusal denklem sistemleri eş zamanlı olarak çözülür (birleştirilir). Deneysel çalışmalarda agar-tuz fantomları ile su yastıkları ve $BaTiO_3$ yastıkları kullanılmıştır. Genel olarak yastık, en yüksek fayda için 180° yay açısına ve fantomla aynı yüksekliğe sahip olmalıdır. Ayrıca, yastık fantoma ne kadar yakın olursa, etkisi daha belirgin olmaktadır. Yastık

kalınlığını ve/veya yastığın iletkenliğini arttırmak, DKB kayma miktarını arttırırken, bu parametrelerin aşırı artırılması iletkenlik görüntülerinde hatalara neden omaktadır. Bunun sebebi araştırılmış ve manyetik alanın z-yönündeki teriminin (H_Z) uzaysal türevlerinin ihmal edilebilir olduğu varsayımı yüksek etkili yastık kullanımı ile bozulmaktadır. Diğer taraftan yastık iletkenliği, DKB artefaktının ortadan kaldırılmasında önemli olmayan bir etkiye sahiptir. Önerilen yöntem kullanılarak DKB artefaktı kaldırılmış ve ayrıca oluşturulan iletkenlik görüntülerindeki değerlerin doğruluğu geliştirilmiştir. Kalın su yastıklarının ince olanlardan daha iyi olduğu, yüksek dielektrik yastıklarının ise ince olarak tercih edilmesi gerektiği kanıtlanmıştır. Bu yöntemin sınırlayıcı etkenleri, çoklu uyarımlardan dolayı veri elde süresinin artıyor olması ve H_Z ile ilgili varsayımın yastık parametresi seçimi ile önemli ölçüde bozulmasıdır. İkinci yöntem sadece 1 uyarım gerektiren ve DKB artefaktını düzelten bir çözüm önermektedir. çok kanallı bir almaç sarımının almaç hassasiyetleri arasındaki farkını, her kanal verisindeki DKB bölgelerini değiştirmek için bir araç olarak kullanır. Quadrature olmayan bir sarım için doğruluğunu yitirmesine rağmen, gönderim fazının toplam fazın yarısına eşit olduğu yaklaşımını söyleyen toplam faz varsayımı (TFV) kullanılır ve farklı kanallardan oluşturulan veriler DKB artefaktından muaf iletkenlik görüntüleri oluşturmak için birleştirilir. Sonuçların karşılaştırılacak olursa, ikinci yöntem, DKB artefaktı olmadığı için özgün yöntemden, ve yastık yönteminin gerektirdiği sürenin en az yarısı ile veri alabilmesinden dolayı yastık yönteminden daha üstündür. Bununla birlikte, çok kanallı almaç yöntemi, yanlış faz kullanımından ötürü kesinlikten yoksundur, fakat, sadece komşu dokular arasındaki karşıtlık incelenirken nitel iletkenlik görüntüleme için değerli bir araç olabilir.

Anahtar sözcükler: Manyetik Rezonans Elektriksel Özellik Tomografisi (MREÖT), konveksiyon reaksiyon denklemine dayalı MREÖT (kr-MREÖT), elektriksel özellik görüntüleme, iletkenlik görüntüleme, çok kanallı elektriksel özellik görüntüleme, dielektrik yastık.

Acknowledgement

Although I am raised in an environment inclined to biology and medicine by the parents consisting of a medical doctor and an academician majored in veterinary, I chose to be an electrical and electronics engineer. It was only after the course I took from Prof. Yusuf Ziya İder, that the idea of combining the subject I am interested to with my ambition as an engineer came true as a career opportunity. Throughout the two and a half years studying biomedical, I have always been glad to decide pursuing my career in this field as a researcher.

I am indebted to my supervisor, Prof. Yusuf Ziya İder, not only for helping the decision I made to be an MSc student in the biomedical field, but also for encouraging me to continue further. As a young researcher and a scientist, I admire his determination and wide range of knowledge. I have learnt a lot from his valuable guidance, from his systematic way of thinking, and from the experience he passed on me.

I would like to thank Prof. Ergin Atalar and Prof. Nevzat Güneri Gençer for being my jury members and for their valuable comments.

I want to acknowledge The Scientific and Technological Research Council of Turkey (TÜBİTAK) for providing financial support during my graduate study.

I would like to thank National Magnetic Resonance Research Center (UMRAM) for the possibility to utilize the MRI machine and for providing assistance when I needed.

I wish to extend my thanks to Mürüvet Parlakay for being the most helpful person in administrative works for the past 7 years.

I am grateful to my office mates for providing a warm and happy environment. Special thanks to Dr. Necip Gürler and Dr. Ömer Faruk Oran for their support and guidance since the very beginning of my studies. Yiğit Tuncel and Toygun Başaklar have been very kind and helpful during the years we shared the same

office. I would like to especially thank Gökhan Arıturk, Safa Özdemir and Çelik Boğa for the valuable discussions and conversations we have made on our studies as well as on life itself. I was lucky to have you by my side through the rough paths of the academic life.

Some being there for me more then ten years, each of my best friends, Duygu Şafak, Özge Karaman and İdil Yaranlı has a special place in my heart. I would like to especially thank Sevgi Gökçe Kafalı for staying in Ankara for her MSc studies and being physically there when I need someone to talk to and also for sharing her academic knowledge. I appreciate the support they provide and I believe that they can cheer me up and encourage me to continue no matter how deep I am.

I am more than grateful to Adem Altıntaş for being there for me through my ups and downs and for never letting me down. His unconditional love and support have been motivated me to try harder in my studies and more importantly showed me what is really worth to fight for.

Last but most importantly, I am indebted to my parents, Güler and Gültekin Yıldız for raising me to who I am. I always look up to them as they are honest, sincere and hard-working people and I will follow their steps in life. I couldn't have come through the difficulties I have faced without their love and support. I am honored to be their daughter and more than lucky to have them in my life.

Contents

List of Figures

List of Tables

Chapter 1

Introduction

Magnetic Resonance Imaging (MRI) has proved its importance as a medical diagnostic tool since the development of Nuclear Magnetic Resonance in 1980s. One of the reasons that MRI gained its popularity is the fact that it does not emit ionizing radiation in contrast to the medical imaging tools such as computer-aided tomography (CT) and positron emission tomography (PET) scans. Therefore, it is less hazardous to the patient and this feature of MRI becomes more significant when there is a need to be continuously imaged such as the stage control of a malignant tissue. Another reason is that MRI contributes the diagnosis with wide range of contrast images that other medical tools cannot provide. By varying the acquisition parameters, different contrast images as well as quantitative images can be obtained. In this thesis, a particular form of a contrast mechanism, imaging of the conductivity, will be examined by the use of phantoms that simulate the tissue properties. In the following sections, first, a summarized review regarding the electrical property imaging and Magnetic Resonance Electrical Properties Tomography (MREPT) will be given and then the motivation of the cr-MREPT method will be provided. Low convective field (LCF) artifact issue in cr-MREPT method will be explained, and the purpose and scope of the thesis will be presented. At the end of this chapter, organization of the following chapters will be stated.

1.1 Electrical Property Imaging

Imaging the electrical properties, EPs, (σ is the conductivity and ϵ_r is the relative permittivity or the dielectric constant) of tissues is beneficial in many respects. Conductivity imaging provides clinically important information due to conductivity differences among healthy tissues and also between healthy and malignant tissues [1, 2]. Transcranial magnetic stimulation [3], hyperthermia treatment [4], and radiofrequency (RF) ablation [5] are examples of therapy monitoring applications requiring EP information. In high field MRI, EP information is helpful to calculate the specific absorption rate [6], which is related to the tissue heating and is a very essential subject of MRI safety.

Previous EP imaging techniques aimed to measure tissue properties at low frequencies such as 1 kHz-1 MHz. In electrical impedance tomography (EIT), surface electrodes are attached to the body, and the currents are injected and measured from these electrodes [7–11]. Magnetic induction tomography (MIT), on the other hand, generates the currents to be given to the body by an external transmitter coil and measures the magnetic field due to induced currents inside the body by a receiver coil [12]. However, both methods produce low resolution impedance maps especially while imaging deeper in the body. To overcome this issue, magnetic resonance electrical impedance tomography (MREIT) has been proposed [13–21]. Main difference of MREIT from EIT is that the magnetic field generated inside the body is measured using MRI and not the surface electrodes. Although MREIT has a higher spatial resolution, amount of the injected current is still an issue in clinical applications due to undesired muscle or nerve stimulations.

The idea of calculating EPs at the Larmor frequency of an MR system has been proposed by Haacke in 1991 [22] and applied for the first time by Wen in 2003 [23]. Magnetic resonance electrical properties tomography (MREPT) has been reintroduced and extensively analyzed by Katscher in 2009 [6]. MREPT is based on the fact that EPs perturb the RF magnetic field and therefore they can be extracted from the information buried in the RF magnetic field. Haacke has developed the first formula for the relationship between admittivity ($\gamma = \sigma + i\omega\epsilon$)

and the RF magnetic field as follows:

$$\gamma = \frac{\nabla^2 \mathbf{H}^+}{i\omega\mu \mathbf{H}^+} \tag{1.1}$$

where ϵ is permittivity, μ is permeability, ω is the Larmor frequency, and $H^+ = H_x + iH_y$ is the complex left-hand rotating magnetic field, or in other words, the transmit magnetic field. This conventional MREPT method is point-wise, prone to noise, and more importantly, it assumes locally constant EP values, or local homogeneity assumption (LHA), which results in error at the tissue boundaries where EPs change abruptly.

Several studies to overcome the boundary artifact issue have been conducted. Gradient based electrical properties tomography (g-EPT) uses a multi-channel transceiver RF coil and obtains the gradients of EPs, which are then integrated starting from a seed-point [24]. Contrast Source Inversion based EPT (CSI-EPT) tries to minimize the difference between the measured and the modeled H^+ data iteratively to find the EPs [25]. Hafalir has proposed the convection-reaction equation based MREPT (cr-MREPT) where the relation between EPs and the H^+ is modeled as a convection-reaction partial differential equation (PDE) [26] .

1.2 LCF Artifact in MREPT

In cr-MREPT method, when the convective field of the convection-reaction equation is very low, the solution for EPs displays artifacts. This region is called the Low Convective Field (LCF) region and the resulting distortion is called the LCF artifact. While being a spot-like artifact in simulation studies, the effect of LCF is increased due to noise in experimental data, resulting in a disturbed region, generally in the center of the object. g-EPT also suffers from a similar artifact, mentioned as a "global bias" in [27]. Also, it is observed in CSI-EPT based methods that low E field regions, which are identical with the LCF regions, result in artifacts [25, 28]. Hafalir proposed a double-excitation method by cutting a portion of the phantom and repeating the data collection, and then combining the two excitation data with different LCF locations. Although it

eliminates the LCF artifact, it would be impractical in a real life application. Another multi-excitation method is presented by Ariturk where a multichannel multi-transmit transverse electromagnetic (TEM) array is used to obtain different H^+ fields with shifted LCF regions [29]. This method however is demanding on the RF amplifiers and requires a multi-transmit coil and system. Gurler proposed a phase-based MREPT, which uses the phase data only and suffers less from LCF artifact [30]. In general, phase-based methods give high contrast conductivity images, but they fail to give the correct values as they assume low B_1^+ magnitude gradients [31, 32].

Regularization, based on introducing an artificial diffusion term in the cr-MREPT PDE, has been proposed to mitigate LCF artifacts [33, 34]. Determination of the value of the regularization parameter (the diffusion constant) is still a major issue in such methods because one has to compromise spatial resolution with elimination of the LCF artifact. Although one may experience complete elimination of the LCF artifact in some numerical simulation cases, it is analyzed in [34] such that LCF artifact reappears when noise is added to the simulated data or when actual noisy experimental data are used .

1.3 Purpose and Scope of the Study

As explained in Section 1.1, EPs and particularly the conductivity imaging is helpful in medical diagnostic aspect as well as RF safety aspect. In the growing society of EPT, MREPT especially has gained more interest due to high spatial resolution that MRI provides. Also it provides a less uncomfortable procedure for a clinical patient as MREPT is non-invasive and requires no electrodes to be attached. Among other MREPT algorithms, cr-MREPT requires less acquisition time unlike [24], less computational burden unlike [25, 28], and less regularization techniques to be applied unlike [35]. However, the MREPT algorithms, which are mentioned earlier and do not use LHA, suffers from an artifact, which is called in cr-MREPT as the LCF artifact that conventional methods do not suffer from. This thesis proposes two methods to circumvent the LCF Artifact issue.

The first method is called the Padding method [28, 36]. Dielectric pads are generally used in high field MRI for B_1^+ shimming purposes [37–40]. Dielectric pads act as a secondary source of magnetic field and therefore the total magnetic field can be altered with specific emplacement of the pads. Especially $BaTiO_3$ (Barium Titanate), which has very high dielectric value in a powder form, is preferred to be used for a padding material as slurry (mixed with water). I have studied with water pads as well as two different $BaTiO_3$ slurry pads, in which the EPs are different. std-MREPT is used to determine the EPs of the prepared slurries. First, the effect of the high dielectric pads on the H^+ field in the object is studied in the simulation environment. These pads are placed on the opposite sides of the object of interest in consecutive experiments such that each excitation set results in LCF regions that are apart from each other. Then, obtained simulation and experimental data, with or without pad, are combined to produce artifact-free conductivity images. A registration problem occurs during the pad alteration when the object itself is moved mistakenly, and this problem is solved by an optimization algorithm called "Genetic Algorithm". Simulation studies and experiments are conducted to validate the proposed method and also to determine the optimum pad character.

The second method to correct the LCF artifact is called the Multichannel Receive method. In a quadrature-excited Birdcage coil (QBC) transceive system, one may obtain 1 data set with 1 LCF region or may place pads to alter the system characteristic and get multiple consecutive experiment data to obtain different data sets with different LCF regions. The latter one, however, lengthens the acquisition time by the factor of the consecutive experiments conducted. I propose to use multichannel receive coil to obtain different data sets, in which the LCF regions differ due to the different receive sensitivities. cr-MREPT uses transceive phase assumption (TPA), which is only valid for quadrature coils. With the use of multichannel receive, TPA fails to validate and the incorrect phase data is used to reconstruct the conductivity images. Although, the reconstructed conductivity images are expected to be inaccurate, the method still provides LCF-free contrast images for conductivity. In addition to eliminating the LCF artifact, this method requires the same time as a QBC transceive system does.

Phantom experiments have been conducted to verify the method, and also the two proposed methods and the original cr-MREPT method is compared to each other in means of acquisition and the resulting conductivity images.

1.4 Organization of the Thesis

This thesis consists of five chapters:

Chapter 2 explains the theoretical background of the MREPT in general and then cr-MREPT thoroughly. Derivations of the formulas and the assumptions regarding the methods are given. Drawbacks of the conventional algorithm and the cr-MREPT algorithm are discussed. At the end of this chapter, proposed methods to solve the LCF artifact issue are introduced.

Chapter 3 explains one of the proposed methods, which is called the Padding technique. This chapter first presents the effect of the high dielectric and high conductive pads on the H^+ field in an object, then the effect on the LCF region is analyzed. Different data sets with altered pads are combined to reconstruct artifact-free conductivity images and various pad parameters (such as thickness, height, EPs etc.) are inspected to determine the optimum pad structure for MREPT purposes. Simulation and experimental study results are demonstrated and the chapter is concluded with a discussion section.

Chapter 4 explains the other proposed method of this thesis, which is named as multichannel receive technique. It presents an alternative receive technique for the cr-MREPT algorithm, with the use of which the LCF artifact elimination is achieved in the same acquisition time as the conventional cr-MREPT. Methodology and the experimental studies for the second method are presented. The drawbacks and the advantages of the two proposed methods and also the conventional cr-MREPT method are compared and this chapter concludes with a discussion section.

Chapter 5 summarizes the proposed methods and is concluded with the possible future directions.

Chapter 2

Theoretical Background

This chapter gives the theoretical basis of MREPT methods. Starting from the electromagnetic derivations, first the conventional MREPT equation will be provided and its drawbacks will be examined. Then, cr-MREPT PDE will be derived step by step. Advantages and the limitations of this algorithm will be presented. The chapter will end with a concise description of the methods that are proposed by this thesis as solutions for the explained issues.

2.1 Magnetic Resonance Electrical Properties Tomography (MREPT)

At the Larmor frequency, the RF coil generates a magnetic field, H, inside the object. Though it is desired to obtain a homogeneous H field, electrical properties, EPs, (σ is the conductivity and ϵ_r is the dielectric permittivity) of the object effects the field and the homogeneity is disturbed. The EPs of the object determine the current flow inside the object and a secondary field is formed, which then perturbs the H field. MREPT aims to find the EPs by employing this perturbation.

To find a relation between the EPs and the magnetic field, one should take the curl of Ampere's law (with Maxwell's addition) and replace the electric field with the magnetic field (using Faraday's law). The formulation will be as follows:

$$-\nabla^2\mathbf{B} = \frac{\nabla\gamma}{\gamma} \times (\nabla \times \mathbf{B}) - i\omega\mu\gamma\mathbf{B} \tag{2.1}$$

where $\mathbf{B}$ is the magnetic flux density, $\mathbf{B} = (B_x, B_y, B_z)$, $\gamma = \sigma + i\omega\epsilon$ is the admittivity, ω is the Larmor frequency, and μ is the magnetic permeability (μ will be taken as μ_0 throughout the thesis). Magnetic flux density and the admittivity are a function of space, $\mathbf{r} = (x, y, z)$.

Local Homogeneity Assumption (LHA) assumes that the EPs are constant. In that case, the $(\frac{\nabla\gamma}{\gamma} \times (\nabla \times \mathbf{B}))$ term in Eq. (2.1) vanishes, and re-writing the equation, it will become as follows:

$$\gamma = \frac{\nabla^2\mathbf{B}}{i\omega\mu\mathbf{B}} \text{ or } \gamma = \frac{\nabla^2\mathbf{H}}{i\omega\mu\mathbf{H}} \text{ equivalently, where } B = \mu H. \tag{2.2}$$

There are left-hand rotating and right-hand rotating RF fields (H^+ and H^- respectively), which are defined as $H^+ = (H_x + iH_y)/2$ and $H^- = (H_x - iH_y)^*/2$ [41]. It is more straightforward to obtain the H^+, which is also called the transmit magnetic field then H^- (the receive magnetic field). Rewriting the Eq. (2.2) in terms of measurable MR quantities, it will become as follows:

$$\gamma = \frac{\nabla^2\mathbf{H}^{\pm}}{i\omega\mu\mathbf{H}^{\pm}} \tag{2.3}$$

Eq. (2.3) will be referred to as the standard MREPT (or std-MREPT) in this thesis and it is the central equation of the conventional MREPT methods [6, 22, 23, 32].

2.1.1 Drawbacks of std-MREPT

There are some limitations with the conventional MREPT methods that restrain it to be used in clinical applications. The most important issue with the

std-MREPT is the boundary artifact. With the assumption of LHA, the method cannot reconstruct the regions with abrupt EP changes such as in the tissue boundaries. At the tissue transitions, an artifact called the "boundary artifact" occurs. Figure 2.1 displays the conductivity map of a simulation phantom and the corresponding std-MREPT reconstruction. Boundary artifacts can be seen clearly between the different tissues in Figure 2.1.b. This artifact becomes significant with more complex structures such as brain.

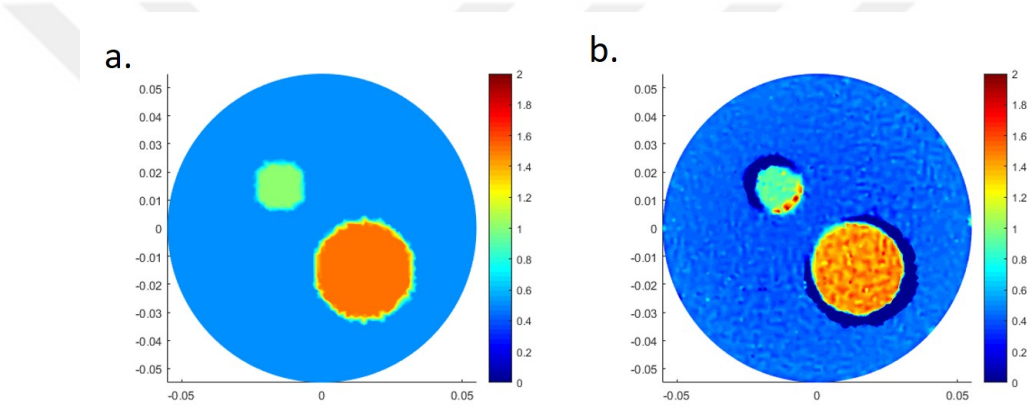

Figure 2.1: a. Real conductivity map (S/m) of the simulation phantom, b. std-MREPT conductivity (S/m) reconstruction of the simulation phantom

While solving Eq. (2.3), one needs to know both the magnitude and the phase of H^+ (or H^-). There are several B_1^+ mapping techniques [42–44], from which B_1^+ magnitude can be obtained directly. However, B_1^+ phase, ϕ^+, is not as easy to acquire. MR signal has the component of transcieve phase, ϕ_{tr}, which is the summation of transmit and the receive phases, and only ϕ_{tr} can be obtained. Many investigators use QBC for both transmit and receive and approximate the transmit sensitivity to the receive sensitivity ($B_1^+ \approx B_1^-$) and therefore $\phi^+ \approx \phi^-$, and $|B_1^+| \approx |B_1^-|$. The transmit phase can be written as $\phi^+ \approx \phi_{tr}/2$ and this approximation is called the transcieve phase assumption (TPA) [6].

TPA has been studied in [45], and it is concluded that with elliptical objects, or non-circular in general, TPA loses its validity. At high field strengths or non-quadrature coils, TPA is not valid anymore.

Another essential issue is the noise level. Since the Laplacian operator is

needed within the MREPT equation, high noise levels distort the results easily. Additional acquisitions for higher SNR requires additional time, especially for B_1^+ mapping, which would be undesired for clinical use. Using low pass filters, on the other hand, reduces the resolution in general. Resolution of phase-based and conventional cr-MREPT has been analyzed in [34, 46].

2.2 Convection-Reaction Equation based MREPT (cr-MREPT)

Trying to solve the boundary artifact issue and to get rid of the LHA, Hafalir has proposed a convection-reaction equation based formulation for MREPT [26], in which the gradient term that has been excluded in the conventional method is also included back.

2.2.1 Formulation of cr-MREPT

The derivation of the cr-MREPT PDE is given in this section.

Substituting μH^+ instead of B, x- and y- components of Eq. (2.1) can be written as:

$$-\nabla^2 H_x = \frac{1}{\gamma}\left[\frac{\partial\gamma}{\partial y}\left(\frac{\partial H_y}{\partial x}-\frac{\partial H_x}{\partial y}\right)-\frac{\partial\gamma}{\partial z}\left(\frac{\partial H_x}{\partial z}-\frac{\partial H_z}{\partial x}\right)\right]-i\omega\mu\gamma H_x \tag{2.4}$$

$$-\nabla^2 H_y = \frac{1}{\gamma}\left[\frac{\partial\gamma}{\partial z}\left(\frac{\partial H_z}{\partial y}-\frac{\partial H_y}{\partial z}\right)-\frac{\partial\gamma}{\partial x}\left(\frac{\partial H_y}{\partial x}-\frac{\partial H_x}{\partial y}\right)\right]-i\omega\mu\gamma H_y \tag{2.5}$$

Multiplying Eq. (2.5) with i and adding to Eq. (2.4), by using the H^+ and H^- definitions, we obtain

$$
\begin{aligned}
-2\nabla^2 H^+ = &-\frac{1}{\gamma}\frac{\partial \gamma}{\partial x} i \left(\frac{\partial H_y}{\partial x} - \frac{\partial H_x}{\partial y} \right) - \frac{1}{\gamma}\frac{\partial \gamma}{\partial y} \left(-\frac{\partial H_y}{\partial x} + \frac{\partial H_x}{\partial y} \right) \\
&- \frac{1}{\gamma}\frac{\partial \gamma}{\partial z} \left(2\frac{\partial H^+}{\partial z} - \frac{\partial H_z}{\partial x} - i\frac{\partial H_z}{\partial y} \right) - 2i\omega\mu\gamma H^+
\end{aligned}
\tag{2.6}
$$

Using $\nabla \cdot \mathbf{H} = \dfrac{\partial H_x}{\partial x} + \dfrac{\partial H_y}{\partial y} + \dfrac{\partial H_z}{\partial z} = 0$ equality and again the H^+ and H^- definitions, $\left(\dfrac{\partial H_y}{\partial x} - \dfrac{\partial H_x}{\partial y} \right)$ term can be modified as:

$$
\begin{aligned}
\frac{\partial H_y}{\partial x} - \frac{\partial H_x}{\partial y} &= \frac{\partial H_y}{\partial x} - \frac{\partial H_x}{\partial y} - i\left(\frac{\partial H_x}{\partial x} + \frac{\partial H_y}{\partial y} + \frac{\partial H_z}{\partial z} \right) \\
&= -2i\left(\frac{\partial H^+}{\partial x} - i\frac{\partial H^+}{\partial y} + \frac{1}{2}\frac{\partial H_z}{\partial z} \right)
\end{aligned}
\tag{2.7}
$$

Substituting Eq. (2.7), Eq. (2.6) becomes:

$$
\begin{aligned}
-\nabla^2 H^+ = &-\frac{1}{\gamma}\frac{\partial \gamma}{\partial x} \left(\left(\frac{\partial H^+}{\partial x} - i\frac{\partial H^+}{\partial y} \right) + \frac{1}{2}\frac{\partial H_z}{\partial z} \right) \\
&- \frac{1}{\gamma}\frac{\partial \gamma}{\partial y} \left(i\left(\frac{\partial H^+}{\partial x} - i\frac{\partial H^+}{\partial y} \right) + \frac{i}{2}\frac{\partial H_z}{\partial z} \right) \\
&- \frac{1}{\gamma}\frac{\partial \gamma}{\partial z} \left(\frac{\partial H^+}{\partial z} - \frac{1}{2}\frac{\partial H_z}{\partial x} - \frac{i}{2}\frac{\partial H_z}{\partial y} \right) - i\omega\mu\gamma H^+
\end{aligned}
\tag{2.8}
$$

Dividing Eq. (2.8) by γ and defining $u = 1/\gamma$, the cr-MREPT PDE can be written as:

$$
\mathbf{C} \cdot \nabla u + \nabla^2 H^+ u - i\omega\mu H^+ = 0 \tag{2.9}
$$

where

$$
\nabla u = \begin{bmatrix} \dfrac{\partial u}{\partial x} \\ \dfrac{\partial u}{\partial y} \\ \dfrac{\partial u}{\partial z} \end{bmatrix} = \begin{bmatrix} -\dfrac{1}{\gamma^2}\dfrac{\partial \gamma}{\partial x} \\ -\dfrac{1}{\gamma^2}\dfrac{\partial \gamma}{\partial y} \\ -\dfrac{1}{\gamma^2}\dfrac{\partial \gamma}{\partial z} \end{bmatrix} \text{ and } \mathbf{C} = \begin{bmatrix} C_x \\ C_y \\ C_z \end{bmatrix} = \begin{bmatrix} \dfrac{\partial H^+}{\partial x} - i\dfrac{\partial H^+}{\partial y} + \dfrac{1}{2}\dfrac{\partial H_z}{\partial z} \\ i\dfrac{\partial H^+}{\partial x} + \dfrac{\partial H^+}{\partial y} + \dfrac{i}{2}\dfrac{\partial H_z}{\partial z} \\ \dfrac{\partial H^+}{\partial z} - \dfrac{1}{2}\dfrac{\partial H_z}{\partial x} - \dfrac{i}{2}\dfrac{\partial H_z}{\partial y} \end{bmatrix}
$$

This is a diffusion-convection-reaction equation with null diffusion term. $\mathbf{C}$ is the convective field and note that $C_y = iC_x$, and $\nabla^2 H^+ u - i\omega\mu H^+$ is the reaction part.

Although, H^+ is measurable in MRI, H_z cannot be measured. Using a transverse RF excitation field with a volume birdcage coil, in the center slices, derivatives of H_Z are significantly smaller than the derivatives of H^+ and therefore they are neglected by many investigators [6]. Also, in cylindrical phantoms where there is no change in EPs along z-direction, derivative of u in z-direction becomes zero and Eq. (2.9) simplifies to its 2D form:

$$\mathbf{F} \cdot \bar{\nabla} u + \nabla^2 H^+ u - i\omega\mu H^+ = 0 \tag{2.10}$$

where $\bar{\nabla} u = \begin{bmatrix} \dfrac{\partial u}{\partial x} \\ \dfrac{\partial u}{\partial y} \end{bmatrix}$, $u = \dfrac{1}{\sigma + i\omega\epsilon_0\epsilon_r}$ and $\mathbf{F} = \begin{bmatrix} F_x \\ F_y \end{bmatrix} = \begin{bmatrix} \dfrac{\partial H^+}{\partial x} - i\dfrac{\partial H^+}{\partial y} \\ i\dfrac{\partial H^+}{\partial x} + \dfrac{\partial H^+}{\partial y} \end{bmatrix}$.

Assuming local homogeneity ($\bar{\nabla} u = 0$), the convection term is neglected and the Eq. (2.10) reduces to

$$u = \frac{i\omega\mu H^+}{\nabla^2 H^+} \tag{2.11}$$

Eq. (2.11) is in fact the same as the Eq. (2.3) with the change of $u = 1/\gamma$.

2.2.2 Advantages and Drawbacks of cr-MREPT

There has been achieved a lot with cr-MREPT in Electrical Property Imaging studies. First and foremost, the boundary artifact issue is resolved. While the conventional methods are point-wise and prone to noise, the cr-MREPT method is a global method such that it finds the solution for all pixels simultaneously and considers the constraining effects of neighboring pixels on each other, so that it is more robust against noise.

However, there are some limitations of the cr-MREPT method as well. TPA issue is not addressed with cr-MREPT and the necessary transmit phase for the

cr-MREPT PDE is also found with TPA as the conventional method. Most importantly, there is the LCF artifact issue. When $|F_X|$ is very low, the solution for u displays artifacts. This region is called the Low Convective Field (LCF) region and the resulting distortion is called the LCF artifact. While being a spot-like artifact in simulation studies, the effect of LCF is increased due to noise in experimental data, resulting in a disturbed region, generally in the center of the object. Figure 2.2 displays the $|F_X|$ and the LCF region, as well as the conductivity image reconstructed with the cr-MREPT method. LCF artifact can be seen approximately at the center of the image, where the LCF region approximately sits with respect to the object. The real conductivity map regarding the reconstruction is given in Figure 2.1.

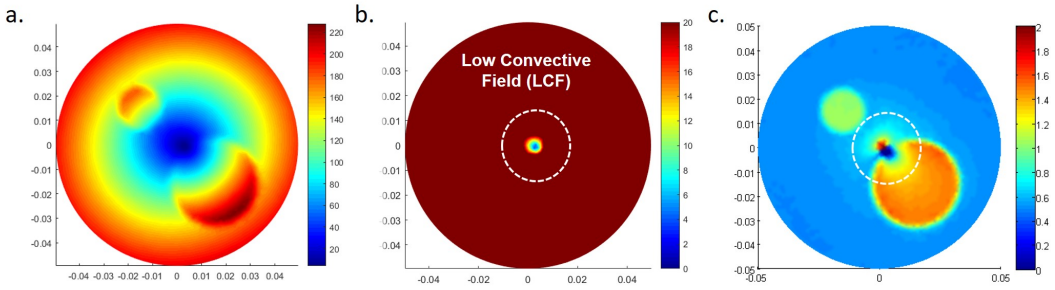

Figure 2.2: a. Convective field ($|F_X|$), b. Low Convective Field (Color scaled version of the image in a.), c. Conductivity image (S/m) reconstructed with cr-MREPT

2.3 Proposed Methods

To obtain LCF artifact-free conductivity maps, two methods have been proposed in this thesis.

Hafalir repeated the excitation by cutting a portion of the phantom and then combined the two data [26]. In spite of eliminating the LCF artifact, cutting a body part for imaging is not applicable at all. Schmidt proposed improving a CSI-based method with the use of high dielectric pads and analyzed in the simulation environment [28]. One of my proposed methods is the

"Padding Technique", which aims to eliminate the LCF artifact in conventional cr-MREPT by using dielectric pads. LCF-free conductivity images are possible by double-excitation, in expense of the acquisition time. This method will be discussed in the next chapter.

The other proposition is the "Multichannel Receive Technique". The difference between the multichannel receive data due to the receive sensitivity is used as a means to shift LCF regions without the need of extra acquisition time. LCF-free reconstructions are possible with this method in expense of the accuracy. This method will be discussed in Chapter 4.

Chapter 3

Padding technique

3.1 METHODS

3.1.1 Simulation Methods

Simulations have been conducted in COMSOL Multiphysics 5.2a (COMSOL AB, Stockholm, Sweden), using the Radio Frequency Module. It computes the wave equation for electrical field in frequency domain with the following formula: $\nabla \times \mu_r^{-1}(\nabla \times \boldsymbol{E}) - k_0^2(\epsilon_r - \frac{j\sigma}{\omega\epsilon_0})\boldsymbol{E}$, where μ_r is relative permeability, $\boldsymbol{E}$ is the electric field, k is the wave number, ϵ_r is the relative permittivity, σ is the conductivity, ω is the operation frequency, and then the magnetic field is obtained with the following formula: $\nabla \times \boldsymbol{E} = -i\omega\mu\boldsymbol{H}$. "Scattering Boundary Condition" is used as a boundary condition on a sphere with 0.5775 m radius. Quadrature birdcage coil (QBC) model is used for transmission. The coil is 24 cm in height, 14.5 cm in radius, and has 16 rungs. The QBC coil is excited in the quadrature volume transmit mode where two ports which are spatially 90° apart are driven by voltage sources (100 V rms) with 90° phase offset with respect to each other [47]. Electromagnetic study is performed at 127.7 MHz, the nominal frequency of a 3T MR system. Calculated H^+ is exported with 1 mm resolution.

Simulation Phantoms and Pads

A cylindrical phantom (height=15 cm, radius=6 cm) with two anomalies is designed (Figure 3.1a). Small anomaly has σ=1 S/m and large anomaly has σ=1.5 S/m while background has σ=0.5 S/m. The whole phantom has ϵ_r =80 and μ_r=1. For $-0.5cm < z < 0.5cm$, the mesh size is less than 1.75 mm and the data are taken from the z=0 slice. Mesh is at most 3 mm in the rest of the phantom (Figure 3.1b). In some studies, the anomalies are removed and a homogeneous phantom with ϵ_r=80 and σ=0.5 S/m is obtained. Figure 3.1d displays a 3D head model [47], the conductivity properties of which are shown in Figure 3.1f. Mesh is arranged similar to the cylindrical phantom (Figure 3.1e) and the data are taken from the z=0 slice.

In Figures 3.1a,b, an example pad with 1 cm thickness and 2 mm gap is shown, where it lies along the full height of the object. When pure water pads are simulated, the corresponding material properties are ϵ_r=80 and σ=0 S/m. The 150, 220 and 290 relative permittivity values are meant to represent pads made by different ratios of $BaTiO_3$ and water. Pad in the head model simulation is shown in Figure 3.1d. Head pad is designed to have a shape which would be expected in a real experiment.

3.1.2 Experimental Methods

3.1.2.1 Experimental Phantom Preparation

Cylindrical experimental phantom (height=17 cm, radius=12.5 cm) is used. Background of the phantom is prepared using an agar/saline gel (20 g/L Agar, 2 g/L NaCl, 1.5 g/L $CuSO_4$) and the higher conductive regions are prepared using a saline solution (20 g/L Agar, 6 g/L NaCl, 1.5 g/L $CuSO_4$). Background is expected to have app. 0.5 S/m conductivity where the anomaly regions are expected to have app. 1 S/m [48].

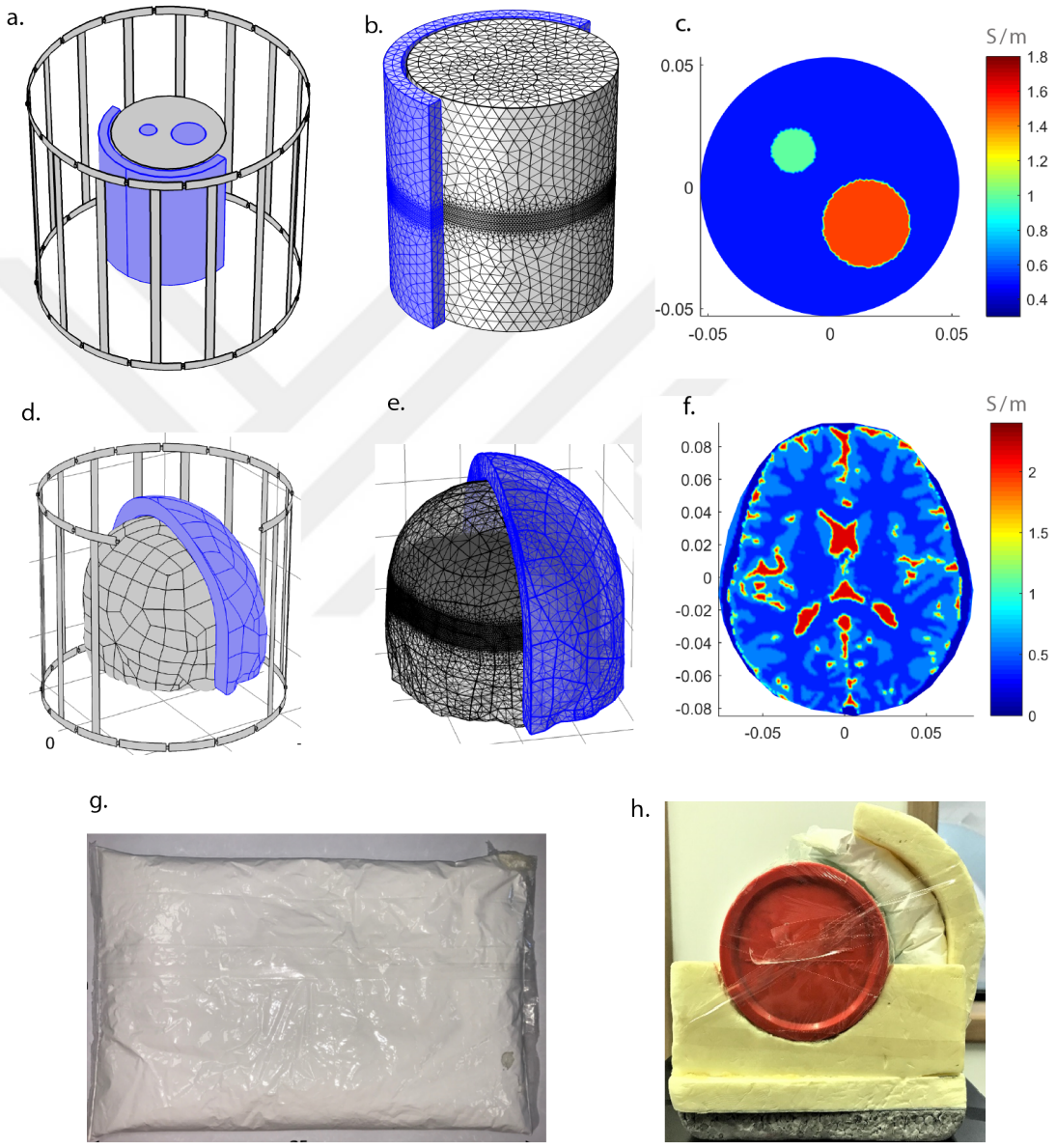

Figure 3.1: Simulation and experimental phantoms and pads. a) QBC, cylindrical phantom and the pad. The pad and the anomaly regions are shown with blue. b) Mesh used for the cylindrical phantom. c) Conductivity values assigned to the cylindrical phantom. d) QBC, the head phantom and the pad. e) Mesh used for the head phantom. f) Conductivity values assigned to the head phantom at the z = 0 slice. g) A $BaTiO_3$ slurry pad. h) An experimental setup with the phantom, the pad and the Styrofoam dock.

3.1.2.2 Pad Preparation

Two kinds of material for padding are considered: water and $BaTiO_3$ slurry. Two different $BaTiO_3$ powders from different vendors (MERCK and Entekno) are used, two slurries with $BaTiO_3$/water weight ratio of 2/1 are prepared. The slurries are collected into polyethylene bags which are hot-sealed (Figure 3.1g).

To fully analyze the effects of the slurries, the dielectric constants of which are measured. Boxes that can carry the fluid character of the slurry are prepared. FR-4 (same as used in PCB) material is used, which would act as parallel plate capacitors. After filling the capacitor boxes with slurries, measuring the capacitance would give us the dielectric constant of the slurry from the following equation: $\epsilon_r = \frac{Cd}{\epsilon_0 A}$, where C is the capacitance, d is the distance and A is the area of the plate. The parallel plate is connected to a network analyzer (Agilent Technologies, E5062A) and the frequency is swept through 500 kHz and 150 MHz so that the slurry characteristic would be fully mapped. In this system, there are inductance in series and resistance in parallel with conductance, therefore, the data cannot be measured directly. "Reactance vs frequency" and "Resistence vs frequency" curves are fitted to find the system characteristics. Although correct values are obtained with pure water, the results of slurries did not converge because the electrical properties of $BaTiO_3$ change with frequency, while being constant in our system model. To directly work within the desired RF range, the Electrical Properties Tomography methods of MRI is used.

Std-MREPT is used to measure the dielectric constant and the conductivity of the resulting slurries. As the $BaTiO_3$ slurry (suspension) is not homogeneous and also some of the $BaTiO_3$ precipitates in time, std-MREPT images are noisy and the obtained H^+ needs to be highly filtered. A 5x5x5 median filter and 5x5x5 Gaussian filter with s.d. of 5 are applied. For two different $BaTiO_3$ slurries, dielectric constant and conductivity are obtained as: for Merck, ϵ_r=187.6 $\pm$ 42.5 (s.d.) and σ=0.05 S/m $\pm$ 0.8 (s.d.); for Entekno, ϵ_r=214.1 $\pm$ 18.9 (s.d.) and σ=1.96 S/m $\pm$ 0.45 (s.d.).

3.1.2.3 Experiment Setup and Registration of Datasets

In general, three consecutive data sets are acquired: without pad (NP-no pad), pad on the left side (LP) and pad on the right side (RP). One important point is that the object should not move between the successive experiments. The phantom is placed on a dock to prevent motion during the experiment (Figure 3.1h), the material for the dock is chosen as Styrofoam such that it is not affecting or get affected by the magnetic field of MRI. Also, another Styrofoam support is placed outside the pad and is fixed after a certain pressure is applied. This procedure is practiced to make the pad thickness even everywhere and to increase the pad effectiveness.

However, while placing and stabilizing the pad, the phantom may still move. To spatially match the datasets, "Genetic Algorithm" method is used as the optimization tool for registration of the images onto each other [49]. Genetic Algorithm is preferred due to its heuristic approach. The edge of NP anatomical image is used as an anchor in general (or any excitation case if NP data is not obtained) and the edge of the second anatomical image is tried to match the first image. Since the edge information is defined as 1s and the background is defined as 0s, the optimization problem of perfectly matching the two edge images is not continuous. Somewhat random but wisely chosen seed points in Genetic Algorithm prevents this problem to converge prematurely.

3.1.2.4 MR Sequences

Experiments are performed using Siemens Tim Trio 3T Scanner (Erlangen, Germany). We use double-angle method [42] for ${B_1}^+$ (or equivalently H^+) magnitude mapping and bSSFP sequence to obtain the ${B_1}^+$ phase. Body QBC is used for transmit and Phased-Array is used for receive in the two gradient-echo sequences which are used for the double-angle method. Sequence parameters are as follows: FoV=170mm, voxel size=1.3mmx1.3mmx3mm, flip angles=60/120, TE/TR=5/1500ms, NEX=4, total duration for DA=26 min.

balanced-Steady State Free Precession (bSSFP) sequence is used due to its speed and high SNR features, also it does not have the additional phase component due to eddy-currents, which makes it a better option than a spin-echo sequence. Body QBC is used both for transmit and receive. Since the transcieve phase approximation is used, the transmit phase is taken as the half of the transcieve phase [6]. bSSFP parameters are: FoV=170mm, voxel size=1.3mmx1.3mmx3mm, flip angle=40, TE/TR=2.23/4.46ms, NEX=32, duration=20 sec.

3.1.3 Numerical methods

Numerical methods are implemented in MATLAB (Mathworks, Natick, MA, USA). H^+, either from the simulation environment or from MRI, is obtained on a regular grid and is interpolated into a triangular mesh. For experiments, diffusion filter, which corresponds to a Gaussian filter with s.d. of 1.7 mm, is used for denoising. Gradients and Laplacian are calculated using the method proposed by Fernandez [50].

The cr-MREPT PDE is discretized to build a linear system of equations as explained in [26], which is also summarized in Appendix. At boundaries we use Dirichlet boundary condition, and boundary values are set to σ=0.5 S/m and ϵ_r=80. Even if the given boundary values are not exactly correct, the values converge to the correct ones within couple of pixels towards the inside of the object. While finding "u", backslash operator of MATLAB is used, which uses the Minimum Norm Least-Squares approach. When the two data sets, or more, are being solved simultaneously, the system of equations are concatenated and again the backslash operator is used.

3.2 RESULTS

3.2.1 Simulation Results

3.2.1.1 Effect of Pad on the RF magnetic field H^+

Simulations are conducted to understand and visualize the effects of pads on the object. The primary rotating electromagnetic field created by the QBC results in current flow within both the pad and the object. The homogeneous phantom together with a (left) pad which has uniform EP of ϵ_r=80 and σ=0 S/m are simulated, and the current distribution in the pad is displayed in Figure 3.2a. Since H^+ is a (left-hand) rotating field, the current distribution also rotates. At different phase instants, current flow direction and intensity change throughout the pad as shown in Figures 3.2a-d.

One can view the current in the pad as one of the sources which generate the H^+ field in the object. To exhibit its contribution, i.e. the effect of the pad, three simulations are conducted in series:

i. The QBC is excited but a pad is not introduced. The magnetic field generated in the object, i.e. the field caused by the coil, H_C^+, is given in Figure 3.2e.

ii. The QBC is excited and also a pad is placed on the left-hand-side of the object. The magnetic field for this simulation, called H_T^+ (T for total), is given in Figure 3.2g. The current distribution induced in the pad is saved to disc.

iii. The QBC is not excited (the driving voltage sources are killed) and the pad is replaced by a volume current source identical to the current distribution saved in the previous step. The field in the object obtained in this case, i.e. the contribution of the pad to the object's magnetic field, H_P^+, is shown in Figure 3.2f.

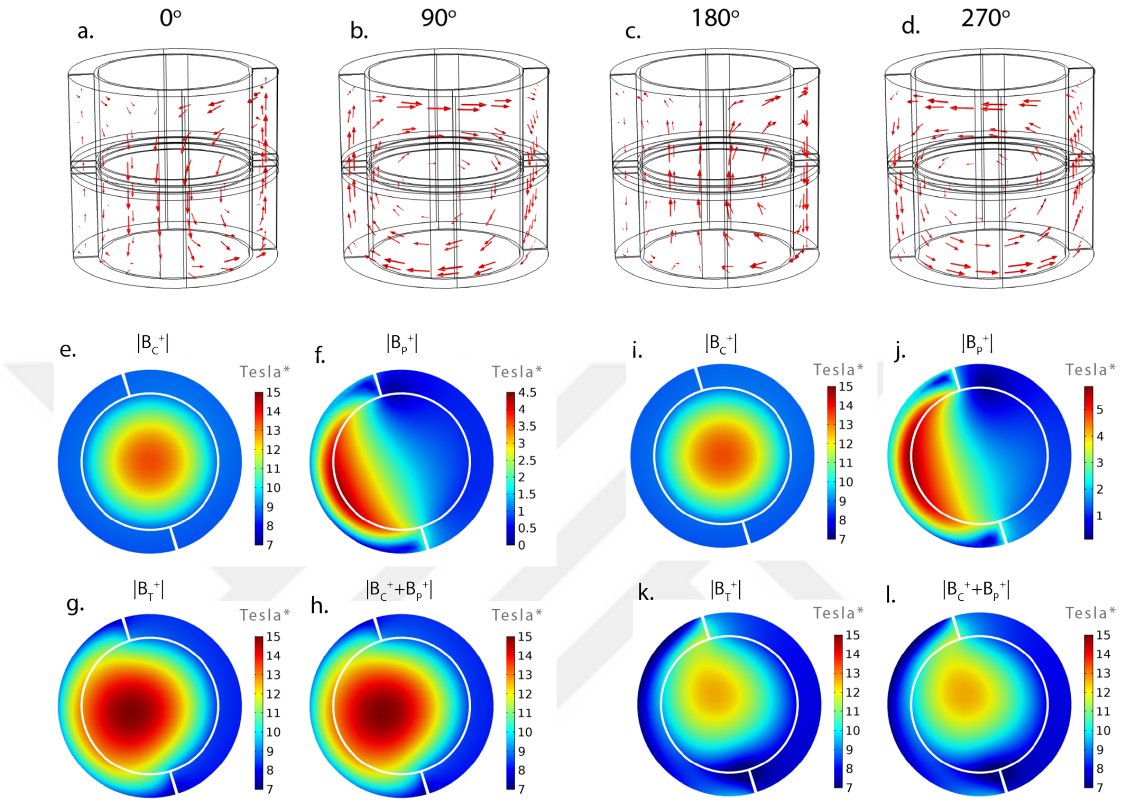

Figure 3.2: Effect of the pad on the H^+ magnitude and the current distribution in the pad. a-d) Current distribution in the pad (ϵ_r=150 ,σ=0 S/m,PT=3 cm and GT=2mm) at 0°, 90°, 180°, and 270° phase instances respectively. e-h) H_C^+,H_P^+, H_T^+, andH_C^++H_P^+ respectively for the same pad. i-l) H_C^+, H_P^+, H_T^+, and H_C^++H_P^+ respectively for another pad (ϵ_r=150, σ=2 S/m,PT=3 cm and GT=2mm). (Tesla* unit refers to the magnetic field strength depending on the power given to the coil)

As shown in Figure 3.2h it is found that H_C^++H_P^+ ≈H_T^+. The extra magnetic field (H_P^+) and the primary magnetic field (H_C^+) are in phase; therefore, the magnetic field close to the high dielectric pad becomes higher in magnitude. The same simulations are repeated with a pad that has uniform EP of ϵ_r=150 and σ =2 S/m. For this case, the same magnetic fields as explained above are shown in Figures 3.2i-l and it is observed that H_T^+ has lower magnitude. This is due to the fact that in this case, the pad has conduction currents due to σ as well as dielectric currents due to ϵ_r. The conduction current and the field generated by it are out of phase with those of ϵ_r and therefore the effect of σ subtracts from the field generated by the coil.

3.2.1.2 Effect of Pad Parameters on LCF Shift

The amount of the LCF shift in the presence of a pad depends in general on the amount of current flowing inside the pad. The parameters that effect the amount of current are the EPs of the pad material, thickness of the pad (PT), angle of the arc that the pad subtends (PA), the height of the pad (PH), and the gap thickness (GT). The parameters are shown in Figure 3.3.

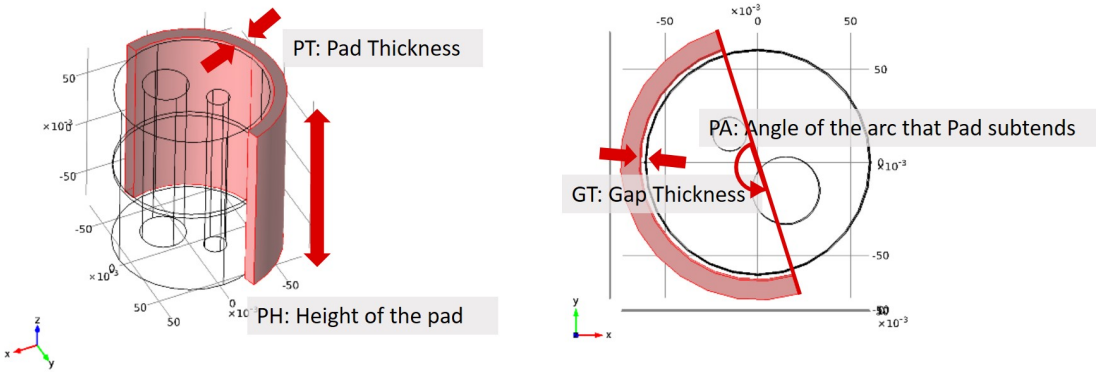

Figure 3.3: Pad parameters

Simulation results for the NP case are shown in Figures 3.4a-c, where the convective field can be seen. The LCF region is almost at the center and the location of the minimum value of the convective field is shown on Figure 3.4c. A LP (left pad) (PT=2 cm, GT= 2mm, σ=0 S/m) is placed and the dielectric constant of the pad is varied. The convective fields are obtained and the locations of the corresponding convective field minimums are displayed in Figure 3.4d. The direction of the LCF shift is towards one end of the pad; moreover, for a fixed pad location changing the pad's dielectric constant, thickness, height and the gap thickness does not alter the direction of the shift but only the amount of it. However, looking to Figure 3.4e, this is not the case for changing the pad's conductivity. Keeping other parameters fixed and varying the conductivity of the pad, one can observe that the locations of the convective field minimums shift almost on an arc centered on the NP (no-pad) minimum location rather than a straight trajectory. A similar difference was observable with the H^+ magnitudes given in Figure 3.2, such that the inclination of H^+ is also different between

pure-dielectric and conductive-dielectric pads.

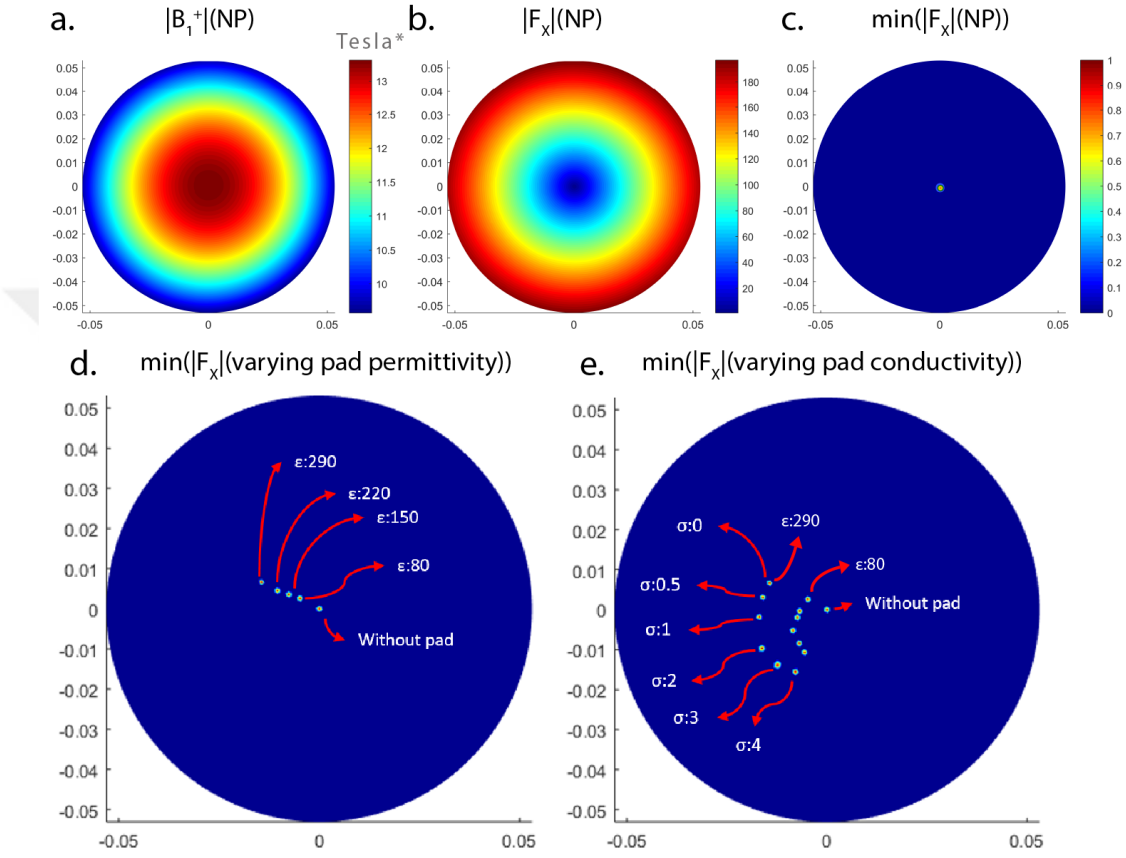

Figure 3.4: Effect of the EPs of the pad on the LCF shift. For homogeneous phantom without a pad, a) magnitude of H^+, b) magnitude of the convective field ($|F_X|$), and c) location of the minimum value of $|F_X|$. d) Locations of the minimum values of $|F_X|$ formed by the pads with different ϵ_r. e) Locations of the minimum values of $|F_X|$ formed by the pads with different σ (S/m); inner points are for ϵ_r=80 and the outer points are for ϵ_r=290 pads.

Figures 3.5a-d display the dependence of the amount of LCF shift on the thickness of the pad, the amount of gap thickness, and the value of the dielectric constant of the pad. LCF shift is calculated as the Euclidean distance between the locations of the convective field minimums of NP and LP. No-gap pads (gap thickness is 0 mm) give rather high shifts than pads with non-zero gap. This is due to the fact that a very low dielectric medium (air) is introduced between the pad and the object when there is a non-zero gap and consequently the effect of the pad is significantly reduced. However, in practice since a gap may be unavoidable, it is more interesting to observe the results of a non-zero gap, and even up to 30 mm shifts are possible with such pads. It can be observed that, for a PT=1 cm pad and GT=2 mm, 3 to 7 mm shifts are possible as ϵ_r is varied from 80 to 290. Similar amount of shifts is achieved with a 2 cm thick pad even when GT is 8 mm. In general, looking through the different PT results, if GT is needed to be increased, then the PT can be increased to balance the amount of the shift. Considering the effect of ϵ_r, the amount of the shift increases with increasing dielectric constant, irrespective of the values of the other parameters. Dependence of LCF shift to ϵ_r seems to be linear with PT=1-2 cm pads; but the incremental effect is more pronounced as ϵ_r is increased for the cases of PT=3-4 cm pads. LCF shift dependence on 1/GT, on the other hand, is not linear, in the sense that, doubling GT will not cause the amount of the shift to be halved. Increasing PT or ϵ_r both act to increase the LCF shift and therefore they can be used as a substitute for each other. For example, a pad with PT=2 cm and ϵ_r=290, and another pad with PT=4 cm and ϵ_r= 150, both cause about 15 mm of LCF shift.

Another set of simulations is conducted to clarify the effect of the angle that the pad subtends. PT=3 cm pad with ϵ_r=150 and GT=2 mm, is wrapped around the phantom with increments of 45° until it reaches the full coverage. The amount of the LCF shift with respect to PA can be seen in Figure 3.5e. Until 180° the amount of the shift increases, whereas after 180° the effect reverses and the amount of the shift decreases since the effects enforced from opposite sides begin to cancel. As 180° of arc angle gives the highest shift, all the pads in this study have 180° of arc angle unless otherwise stated.

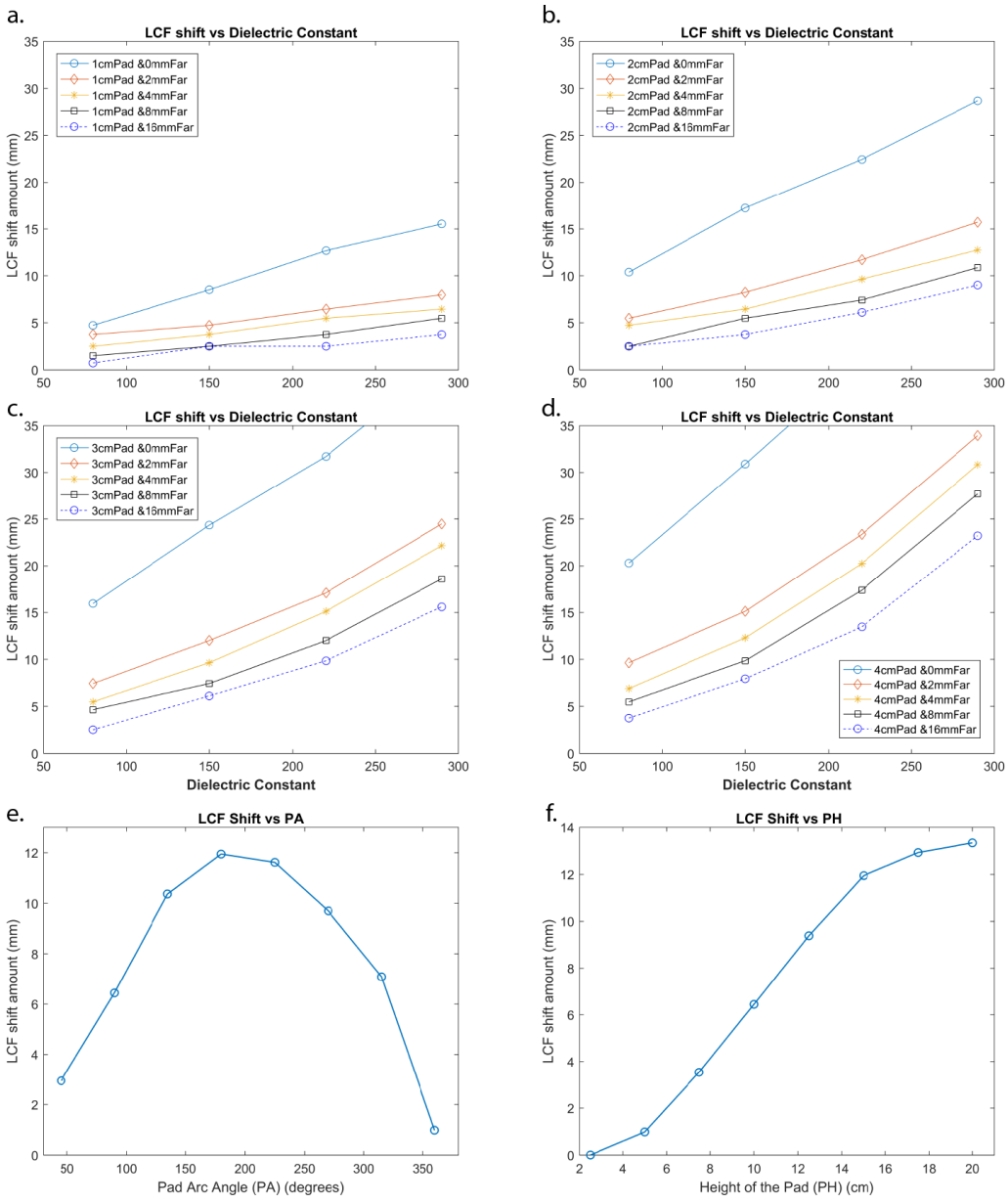

Figure 3.5: Effects of pad parameters on the LCF shift. LCF shift vs dielectric constant of the pad for: a) PT=1 cm, b) PT=2 cm, c) PT=3 cm, and d) PT=4 cm. Results for different GTs are shown on the same graphs. e) LCF shift vs pad angle. f) LCF shift vs pad height.

The height of the pad is also another important factor. Keeping the center of the pad fixed at z=0 (PT=3 cm, GT=2 mm, ϵ_r=150), the height is varied from 2.5 cm to 20 cm with 2.5 cm steps. Although the results are acquired from the center slice, the amount of the LCF shift is still influenced by PH; in fact, with 2.5 cm high pad, no shifts are observed. The relation between PH and the LCF shift amount is displayed in Figure 3.5f. Until 15 cm, which is also the height of the object itself, the relation seems to be almost linear. When PH exceeds the height of the object, increments in the shifts get smaller, though the LCF still shifts further.

3.2.1.3 Effect of Pad Parameters on Combined Conductivity Maps

The main purpose of this study is to determine whether, by using padding, the LCF artifacts in the conductivity maps are eliminated (or reduced) and the conductivity values are more correct. To monitor the effect of the pad parameters on the final conductivity map, reconstructions for individual pad cases are made separately and also for when the data are combined as previously explained.

For conductivity reconstructions, the first phantom model with 2 anomaly regions is used. Figure 3.6 displays H^+ magnitude, convective field, and conductivity maps for left pad with ϵ_r=290, NP, and right pad with ϵ_r=290 (pads have PT=1 cm and GT=2 mm and σ=0 S/m).

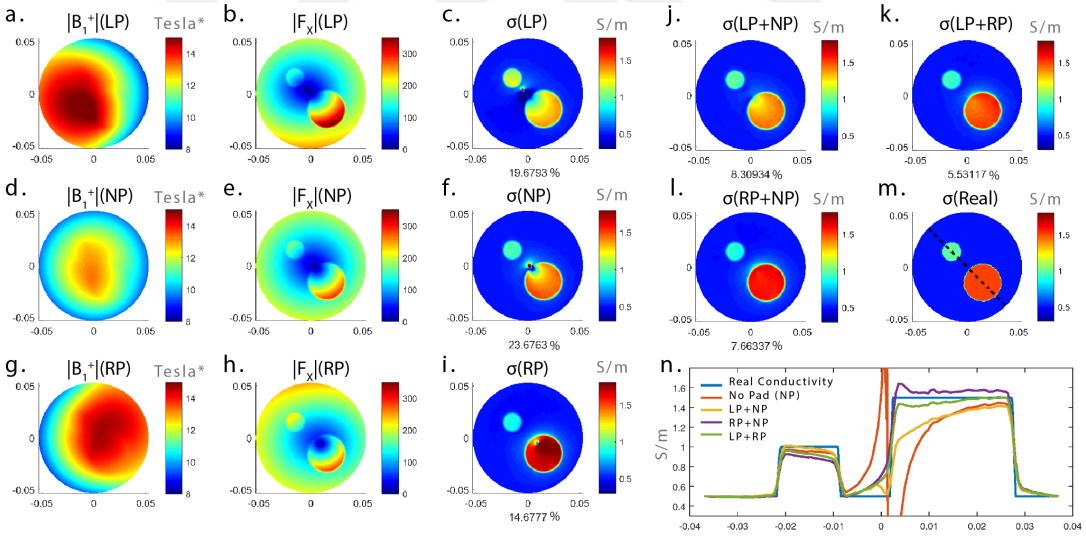

Figure 3.6: Simulation results with the ϵ_r=290, σ=0 S/m,PT=1 cm and GT=2mm pad. a) Magnitude of H^+. b) Magnitude of F_X. c) Reconstructed conductivity image for LP. d-f) The same images for NP. g-i) The same images for RP. j) Reconstructed conductivity image for (LP+NP) combination. k) Reconstructed conductivity image for (RP+NP) combination. l) Reconstructed conductivity image for (LP+RP) combination. m) Real conductivity map. n) Conductivity profiles on the line in m). L^2 errors of the reconstructed conductivity maps (without boundaries) are given below the figures

Dielectric constant of 290 is a relatively high value and the highest that we analyzed, and it succeeds to separate LCF regions (LCF artifacts) from each other to a large extend. Seeing the behavior of LCF artifacts in Figures 3.6c,f,i and

examining them throughout the study, LCF artifacts do not show themselves in a predetermined shape, but instead change their pattern depending on whether the LCF is in or out of an anomaly or whether it coincides with the boundary of an anomaly; the LCF artifact may have patterns like a single dip, a single peak, or both, with the effect fading within couple of pixels or within dozens.

As it is proposed, different data sets are combined to get rid of the LCF artifact: left pad and without pad (LP+NP), right pad and without pad (RP+NP), and left pad and right pad (LP+RP). Figures 3.6j-l display the corresponding combined conductivity results and also the conductivity profiles (on the line given in Figure 3.6m) is plotted in Figure 3.6m. LP+RP combination gives better accuracy and it effectively eliminates the LCF artifact.

A similar simulation result is given in Figure 3.7 for the same pad but with ϵ_r=80. Combined conductivity map for this simulation fails to fully eliminate the artifact while still being more accurate than NP conductivity map. Looking at the LCF artifacts in with and without pad cases, it can be seen that they are not sufficiently far away from each other (the LCF regions overlap) and therefore the artifact is not eliminated completely.

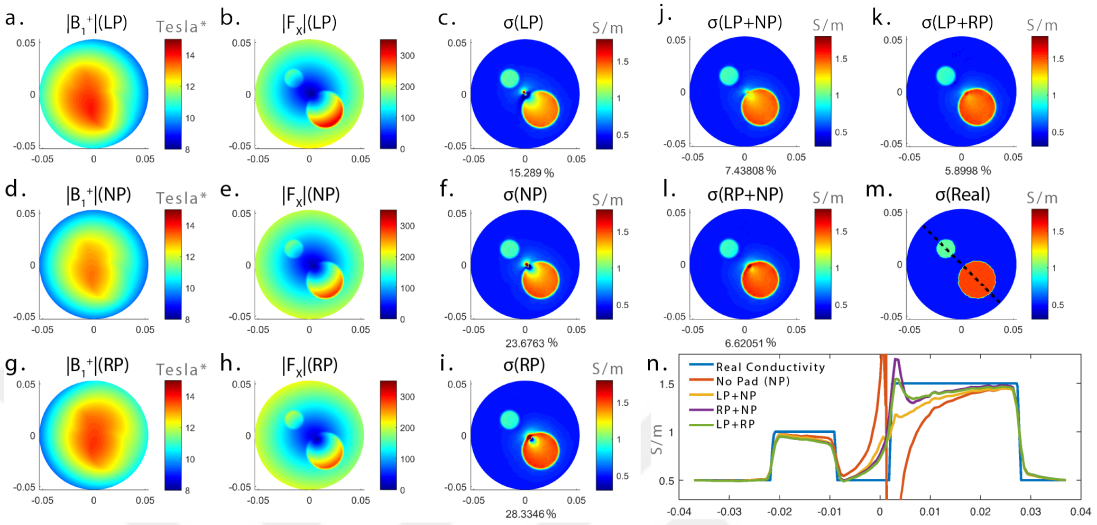

Figure 3.7: Simulation results with the ϵ_r=80, σ=0 S/m, PT=1 cm and GT=2mm pad. a) Magnitude of H^+. b) Magnitude of F_X. c) Reconstructed conductivity image for LP. d-f) The same images for NP. g-i) The same images for RP. j) Reconstructed conductivity image for (LP+NP) combination. k) Reconstructed conductivity image for (RP+NP) combination. l) Reconstructed conductivity image for (LP+RP) combination. m) Real conductivity map. n) Conductivity profiles on the line given in m). L^2 errors of the reconstructed conductivity maps (without boundaries) are given below the figures

LP+RP combination conductivity results for pads with ϵ_r=[80, 150, 220, 290], σ=[0 S/m, 1 S/m] and PT= [1 cm, 3 cm] are provided in Figure 3.8 and the percent L^2-errors are also given below the corresponding images (Percent L^2-error is calculated excluding the anomaly boundaries). Having the lowest dielectric constant of studied EPs, ϵ_r=80 pad provides more accuracy if it is made thicker as opposed to higher dielectric pads. For example using a PT=3 cm and ϵ_r=290 pad gives very poor accuracy, whereas a PT=3 cm and ϵ_r=80 pad gives the highest accuracy among the studied pads. Adding σ=1 S/m to pads, it affects the results minimally when the pad is thin, while it increases the error rate with thicker pads.

The fact that the combined conductivity values are highly distorted with thick high dielectric pads is not what we had expected (see for example in Figures 3.8j,k,n,p). Moreover, it is also unexpected to see that the individual (not combined) conductivity values are also poor in accuracy also in regions other

than the LCF (Figures 3.6c,f,i). It is suspected that neglecting the derivatives of H_Z in Eq. (2.9) may be the reason.

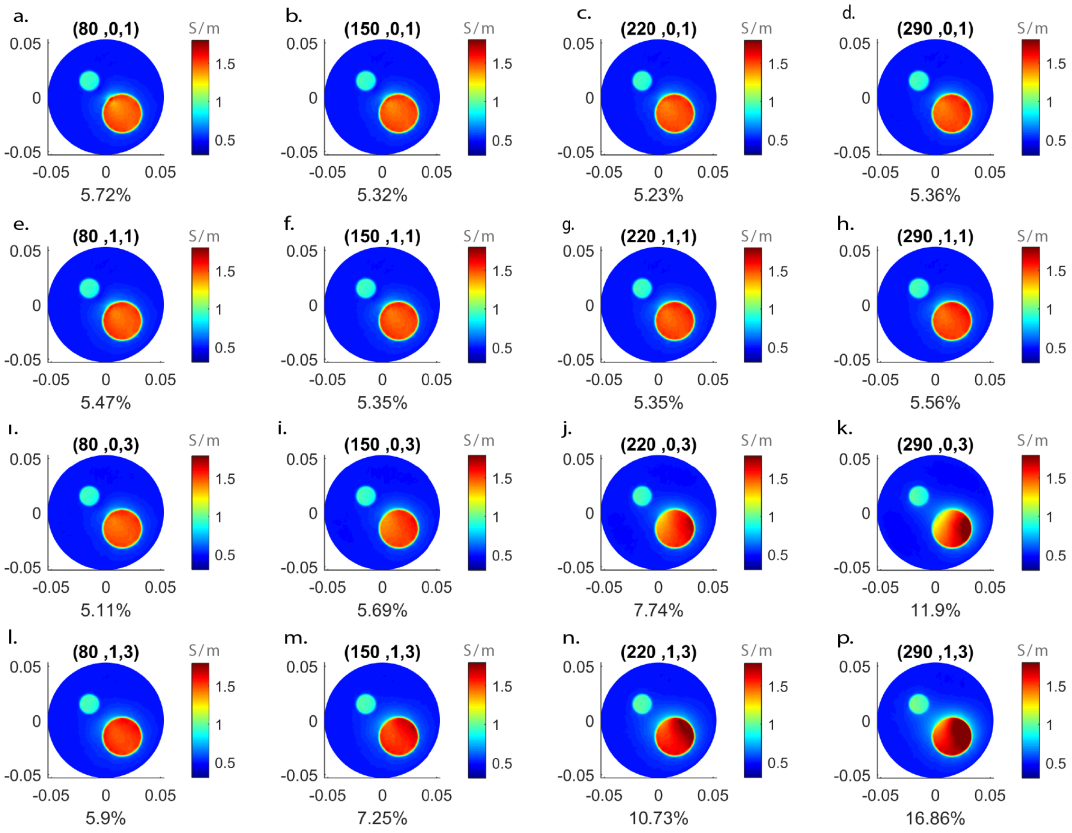

Figure 3.8: Reconstructed conductivity images for (LP+RP) combinations. The properties of the pad used in each simulation are indicated as (ϵ_r,σ,PT) above the figures and the corresponding percent L^2-errors are given below the figures.

To examine the effect of H_Z assumption, reconstruction process is repeated with the H_Z terms included. Figure 3.9 shows the individual and combined conductivity images, where a PT=1 cm ϵ_r=290 σ=0 S/m pad is used. Comparing the individual conductivity images with the ones in Figure 3.6, one can conclude that neglecting the derivatives of H_Z, in fact, causes errors which are even higher with high dielectric pads. With thinner or lower ϵ_r pads, combined conductivity maps are less erroneous, such that combining the data sets overcomes the issues formed by neglecting the H_Z derivatives; however, with thicker and higher ϵ_r pads, derivatives of H_Z become significant and conductivity maps are incorrect. Considering Figure 3.8 again, for ϵ_r=220 or ϵ_r=290, thin pads with PT=1 cm are suitable, but when ϵ_r= 80, a thick pad with PT = 3 cm can be used.

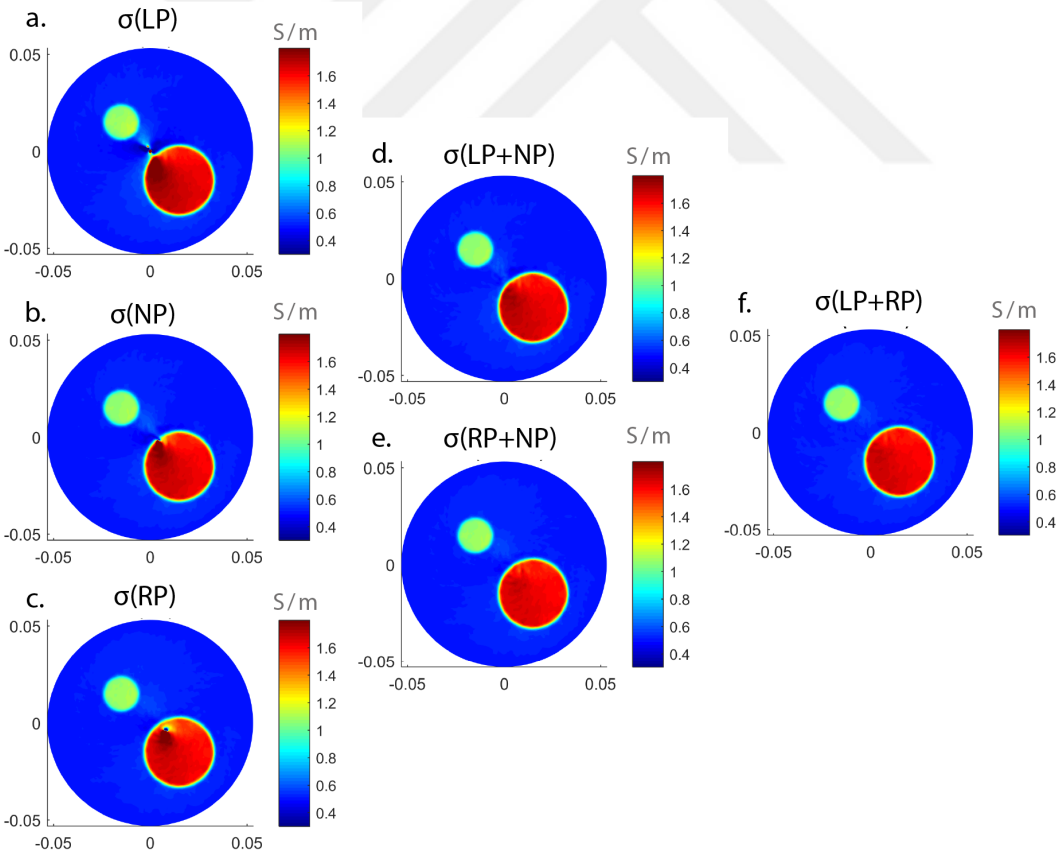

Figure 3.9: Conductivity reconstructions using equation (3), which includes the H_Z derivatives, for the pad and the phantom used in Figure 5. Conductivity images for a) LP, b) NP, c) RP, d) (LP+NP), e) (RP+NP), and f) (LP+RP).

Simulation results using the head simulation model and a pad with PT=2 cm, GT=2 mm, ϵ_r=220 and σ=0 S/m is given in Figure 3.10. Individual and combined conductivity reconstructions, and their profiles along the introduced white line are presented. With this head phantom simulation model, the LCF artifacts in both the LP and RP cases are considerably shifted. The conductivity maps obtained with (LP+RP) and (LP+NP) combinations are satisfactory from the point of view of reduced LCF and accuracy of the conductivity values.

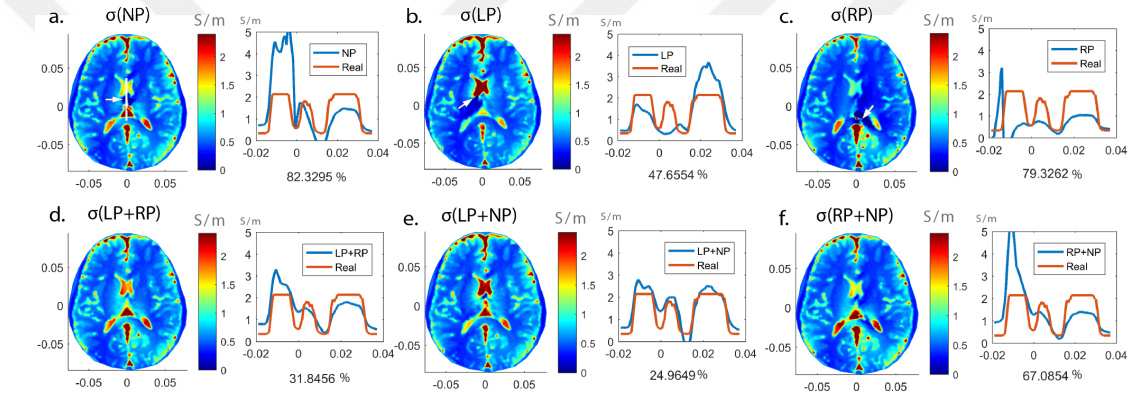

Figure 3.10: Head phantom simulation results. The reconstructed conductivity image for a) NP, b) LP, c) RP, d) (LP+RP), e) (LP+NP), and f) (NP+RP). For each case, conductivity profiles on the white line shown in a) are also given. LCF artifacts in a-c) are indicated with white arrows. L^2 errors of the profiles are given below the figures

3.2.2 Experimental Results

For the two anomaly experimental phantom the bSSFP magnitude images are shown in Figures 3.11a-c for the NP, left water pad and right water pad cases. Pad is approximately 2.5 cm and is approximately 2 mm away from the phantom. Expected conductivity map, Figure 3.11d, is formed using the bSSFP magnitude image. H^+ magnitude images for experiments NP, LP and RP are given in Figures 3.11e-g. Similar to what has been observed in simulations, the inclination of the H^+ field magnitude is towards the pad. Individual (uncombined) conductivity maps, Figures 3.11i-k, have severe LCF artifacts. Figure 3.11h displays std-MREPT result for NP. Figure 3.11l displays the combined (LP+RP)

conductivity map. Conductivity profiles (on the white line given in Figure 3.11d) of NP and LP+RP are plotted in Figure 3.11m. Combined result does not suffer from the LCF artifact and has more accurate results than NP.

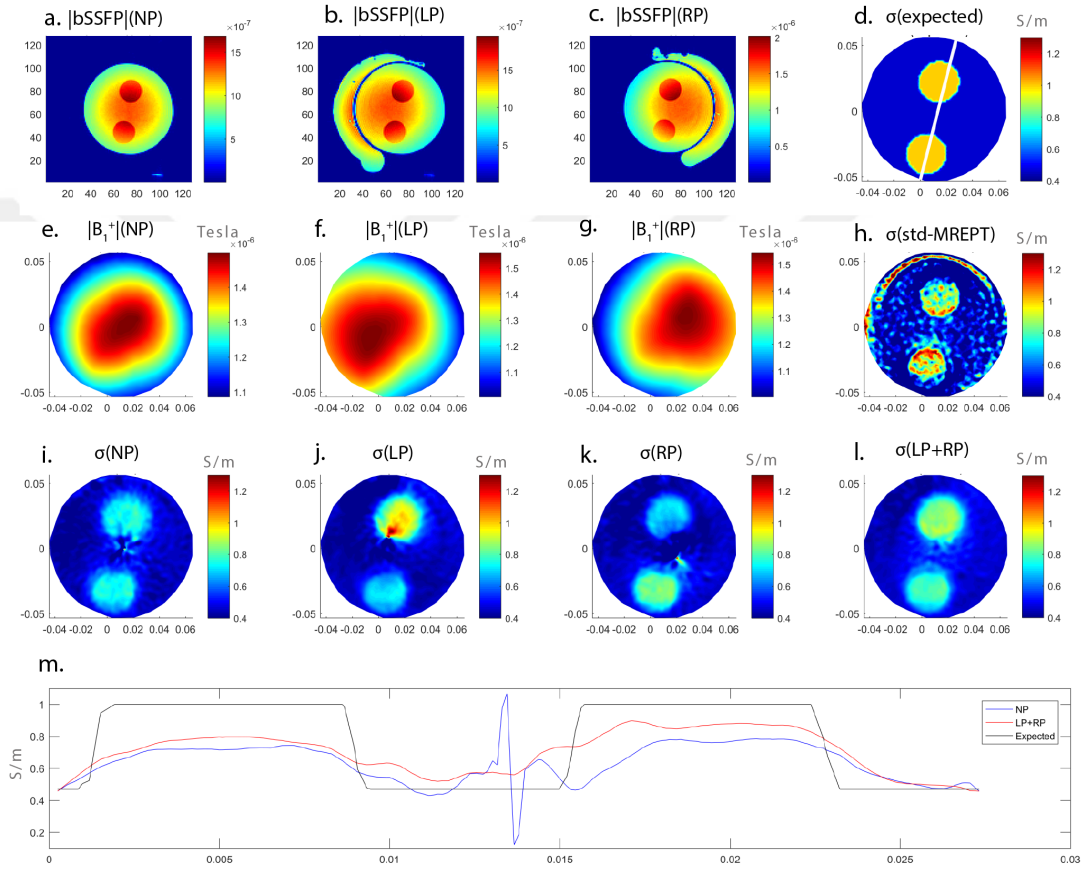

Figure 3.11: Experimental results with a thick water pad. bSSFP magnitude images for a) NP, b) LP, and c) RP. d) The expected conductivity map. H^+ magnitude maps for e) NP, f) LP, and g) RP. h) Conductivity image reconstructed with std-MREPT method. Reconstructed conductivity images with cr-MREPT for i) NP, j) LP, k) RP, and d) LP+RP. m) Conductivity profiles for NP and LP+RP on the line indicated in white in d).

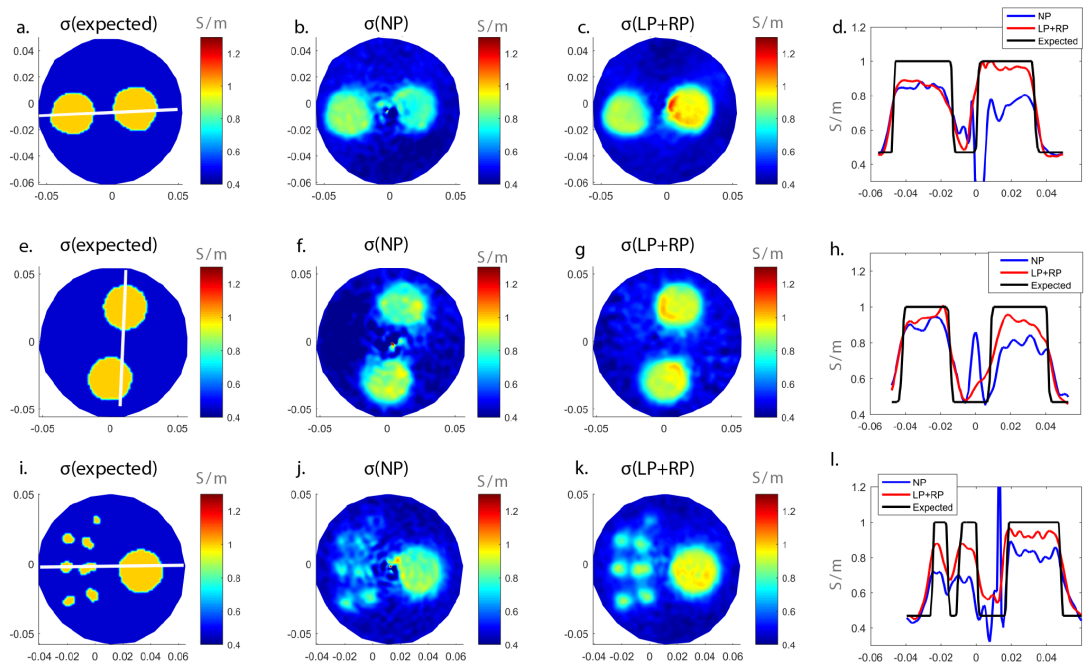

Figure 3.12: Results of thin water pad experiment. Expected conductivity map, reconstructed conductivity map for NP, reconstructed conductivity map for (LP+RP), and their profiles indicated with the corresponding white line respectively. e-h) Same results for non-conductive $BaTiO_3$ (Merck) pad. i-l) Same results for conductive $BaTiO_3$ (Entekno) pad.

Several other experimental results are given in Figure 3.12. Conductivity maps for NP and (LP+RP) are given for each experiment. Also, the reconstructed conductivity profiles on the indicated white lines are shown. Results using a thin water pad (PT=1.5 cm max) are given in Figures 3.12a-d. Even though this is a thin pad and its dielectric constant is not as high as a $BaTiO_3$ slurry, LCF artifact is eliminated with (LP+RP) pad combination. However, since this pad is not very successful at shifting the LCF region the conductivity values of the combination result are not accurate. Non-conductive $BaTiO_3$ slurry pad (PT=3 cm max) experiment results are given in Figures 3.12e-h. (LP+RP) combined conductivity map is free from the LCF artifact and also more accurate than NP. Figures 3.12i-l shows results for a somewhat different phantom in which large and small anomalies are present, and for this case conductive $BaTiO_3$ slurry pad is used. The big anomaly region's conductivity is found just as expected whereas the small anomalies are less accurate but still they have better accuracy

than in the NP reconstruction. Besides, the LCF artifact is eliminated. Even though the simulation results with conductive pads are less accurate than the non-conductive ones, when the experimental results are considered, there are no major differences between them probably due to the presence of experimental noise and also the filters that we have used to combat the noise. The bSSFP magnitude and H^+ magnitude images for NP, LP and RP pad situations for the experiments described in Figure 3.12, are given in Figure 3.13.

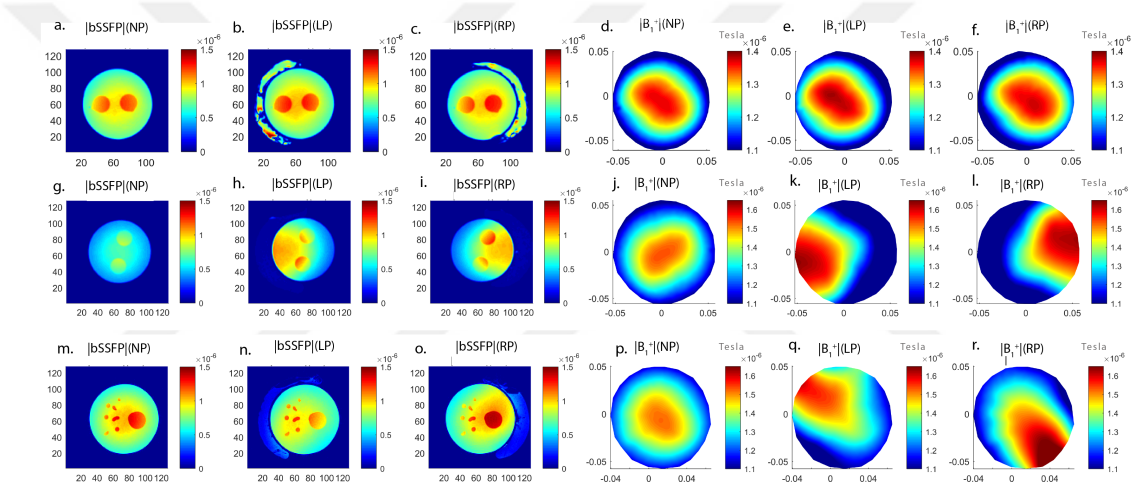

Figure 3.13: bSSFP magnitude images and H^+ magnitude images for the experiments given in Figure 9: a-f) for thin water pad, g-l) for non-conductive BaTiO3 (Merck) pad, and m-r) for conductive BaTiO3 (Entekno) pad.

In additional experiments, we have repeated the bSSFP sequence 32 times in order to achieve more averaging and thus more SNR in the phase of H^+. Results of these experiments, in which a non-conductive BaTiO3 slurry pad is used (PT=3 cm max), are shown in Figure 3.14. Again, LP+RP combinations yield LCF artifact free images. These images are less noisy, compared to the images in Figure 3.12, due to the higher SNR of the data despite the fact that we have used higher cut-off low pass filters for these cases (Gaussian filter with s.d. of 1 mm).

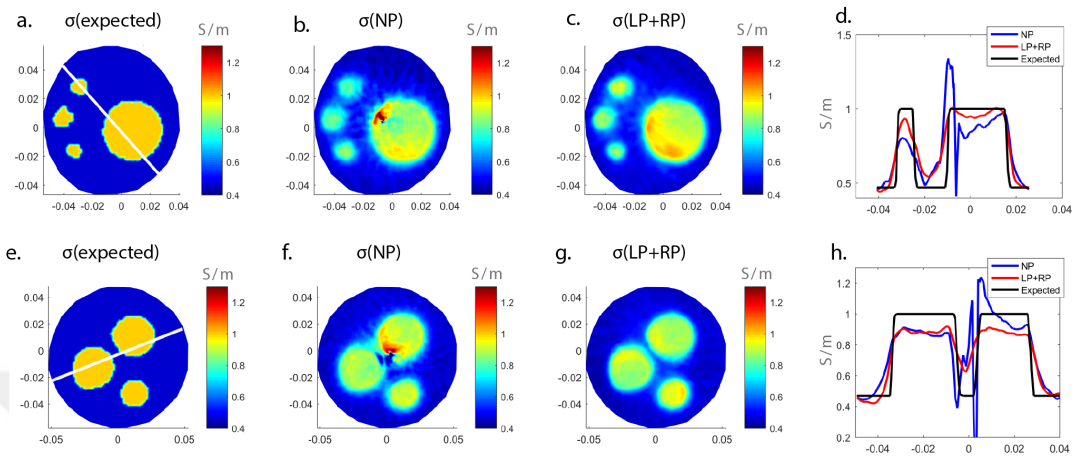

Figure 3.14: Experimental results with high SNR data and non-conductive $BaTiO_3$ pad. a-d) Expected conductivity map, reconstructed conductivity map for NP, reconstructed conductivity map for (LP+RP), and their profiles along the indicated white line for the 4-anomaly phantom. e-h) Same results for the 3-anomaly phantom.

3.3 Discussion

Padding technique has been proposed to improve the cr-MREPT method. Both simulation and experimental results show that the LCF artifact on conductivity maps can be removed with the padding method while also improving the accuracy of the conductivity values. We have also provided information about the mechanism of pad action which may be useful for B_1 shimming studies.

Though the amount of the LCF shift is important so that the LCF regions do not overlap, excessive amount of shift is undesired. This is due to the fact that we neglect the derivatives of the H_Z field and although they are negligible in most of the birdcage studies [6], they become significant with the use of high dielectric pads. The larger the effect of the pad, the more critical H_Z becomes and therefore the error due to neglecting H_Z derivatives in Eq. (2.9) increases. Therefore, if high dielectric pads (e.g. $BaTiO_3$ slurry) are used they must be prepared as thin, or using a thick water pad may be preferred.

An important issue is the time constraint for data acquisition. For each of the

experimental phantoms covered in this work, three different sets of data have been acquired and different pairs are used for the final image reconstruction. However, in general it is observed that, left and right pad combinations give the best results as LCF regions tend to be further away with these pad cases.

Chapter 4

Multichannel Receive Technique

To form complex H^+ (or equivalently ${B_1}^+$) field, magnitude and phase components are obtained separately and then combined just before solving the PDE. The choice of receive coil, whether Phased-array or body QBC, does not alter the obtained B_1^+ magnitude as the transmit field can be found directly with double-angel method [42]; with Phased-array coil, more SNR can be obtained in the same acquisition time with respect to body QBC since more data is obtained through different channels and also Phased-array may be closer to the object such that the signal attenuates less. However, obtaining the transmit field phase is not as straightforward, such that, only transceive phase can be directly found from bSSFP and there are no other method that can construct the transmit phase. Transmit phase is approximated as the half of the transceive phase by many investigators [23, 26, 31], and this is referred to as "Transceive Phase Approximation" (TPA). This approximation fails when non-quadrature coils are used.

It is a wide practice to use body QBC as the transmit coil since it provides homogeneous B_1^+ field at 3 Tesla MR system and to use multichannel Phased-array head coil as the receive coil due to its better SNR characteristics. Application of cr-MREPT in such coil combination may result in erroneous reconstructions due to the failure of TPA. Moreover, using data from a single

channel of a Phased-array results in LCF artifacts, indifferent from LCF artifact issue in original reconstruction (as Hafalir proposed). The padding technique, on the other hand, requires two times the acquisition time to eliminate the LCF artifact.

In this chapter, I propose combining multichannel receive data in order to get rid of LCF artifacts. Transmit phase, ϕ^+, is independent of the receive coil choice and therefore is the same for all data received from body QBC or Phased-array, when the same transmit coil is used. If ϕ^+ could be found directly, then the different channel data would all be the same and the LCF artifacts would also be in the same location and therefore they could not be used for LCF elimination. On the other hand, the receive phase, ϕ^-, will be different for the data received from body QBC and Phase-array due to the difference between a quadrant and a non-quadrant coil. Transceive phase distribution of each channel in Phased-array change due to the coil sensitivity. I make use of the difference that sensitivity of the Phased-array coil provides and see it as a method to alter the location of the LCF artifact. Experiments with phantoms are conducted with the proposed method and also with the padding technique. The results of the padding technique and multichannel receive technique are compared in means of LCF elimination and accuracy, while original reconstructions are also included in the comparison.

4.1 METHODS

Phantom experiments have been conducted with Siemens Tim Trio 3T MR Scanner (Erlangen, Germany).

4.1.0.1 Data Acquisition and MR Sequences

For transmission, body QBC is used for all sequences in all methods. We use double angle method [42] for ${B_1}^+$ magnitude mapping, in which 2 GRE

Table 4.1: Differences in acquisition between the compared techniques (Ph-Arr: Phased-array coil, b-QBC: body QBC)

Method for obtaining the conductivity map	Coil used for RF transmit	Coil used for $\lvert H^+ \rvert$ acquisition	Coil used for ϕ^+ acquisition	Required time (relative)	Different data sets acquired
Original method	b-QBC	Ph-Arr	b-QBC	T	1
The padding technique	b-QBC	Ph-Arr	b-QBC	2T	2
The multichannel receive technique	b-QBC	Ph-Arr	Ph-Arr	T	4

sequences (FoV=170mm, voxel size=1.3mmx1.3mmx3mm, flip angles=60/120, TE/TR=5/1500ms, NEX=4, total duration=26 min.) are acquired through multichannel Phased-array coil for all sequences in all methods.

While obtaining H^+ phase (ϕ^+), original method and the padding technique use body QBC as receive coil. Proposed technique, on the other hand, uses Phased-array receive coil, which is a non-quadrature coil. bSSFP sequence parameters are same in all methods: FoV=170mm, voxel size=1.3mmx1.3mmx3mm, flip angle=40, TE/TR=2.23/4.46ms, NEX=32, duration=20 sec for 1 slice.

Entekno $BaTiO_3$ pad is used on the left and on the right side of the phantom for the padding technique.

Phased-array coil has 12 channels normally but I am using it in circularly polarized mode, in which combinations of 12 channels produces 4 channel data. The difference in acquisition of the compared methods are summarized in Table 4.1.

4.1.1 Numerical Methods

Using a z-independent phantom, conductivity reconstruction is done in 2D.

Numerical methods are implemented in MATLAB (Mathworks, Natick, MA, USA) as explained in previous chapter. Original reconstruction requires only 1 data set, linear system of equations are solved as explained in [26] and backslash operator of MATLAB is used to find u. Conductivity values are then reconstructed according to the relation in (2.10). In padding technique, at least 2 data sets are required and these data sets are solved together as the linear system of equations. With multichannel data, at least 2 different channel data sets are solved together.

4.2 RESULTS

Figure 4.1 shows the $|H^+|$, $\frac{\phi_{tr}}{2}$, and $|F_X|$ images obtained from both body QBC and the Phased-array coil, without the use of padding. Results for Phased-array are given for each channel. Transmit field magnitude is not different for different receive coils as mentioned earlier. Phase, on the other hand, is different for each channel and also from the one received from body QBC. Convective fields are also given in Figure 4.1.e-f. While the LCF region is approximately at the center for the QBC-receive data, the LCF locations are different for each Phased-array-receive channel data.

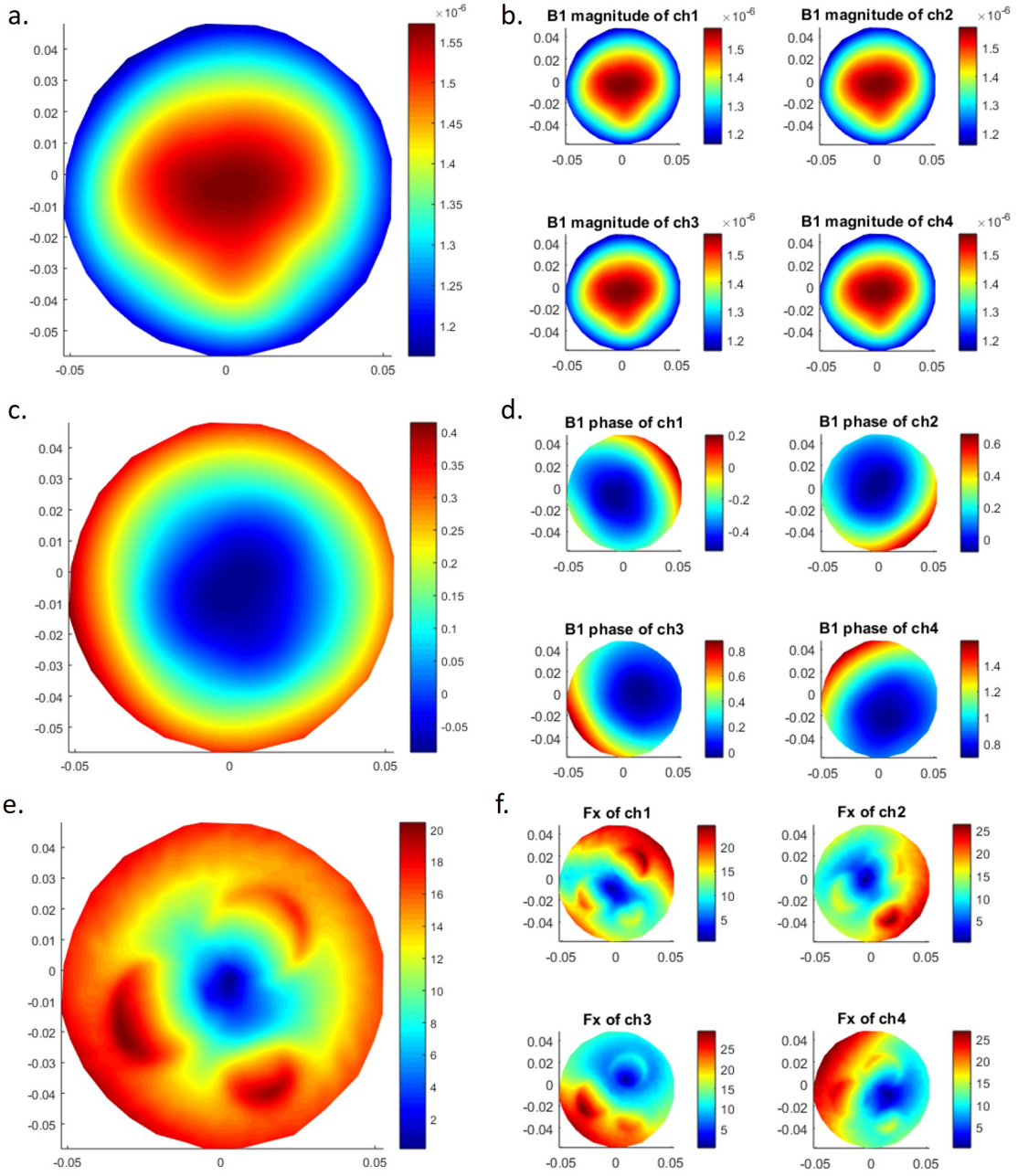

Figure 4.1: a. $|H^+|$ (T) obtained from body QBC, b. $|H^+|$ (T) obtained from Phased-array, c. $\frac{\phi_{tr}}{2}$ obtained from body QBC, d. $\frac{\phi_{tr}}{2}$ obtained from Phased-array, e. $|F_X|$obtained from body QBC, f. $|F_X|$ obtained from Phased-array

Figure 4.2 displays the reconstructed conductivity maps for original method, for LP and RP, and for each channel of the Phased-array-receive data. Each individual case has LCF artifact. Shift in the LCF artifact that the $BaTiO_3$ pad creates is somewhat more pronounced than of the multichannel data. Non-consecutive channels shift the LCF regions to the opposite directions and therefore are better candidate to use in combinations.

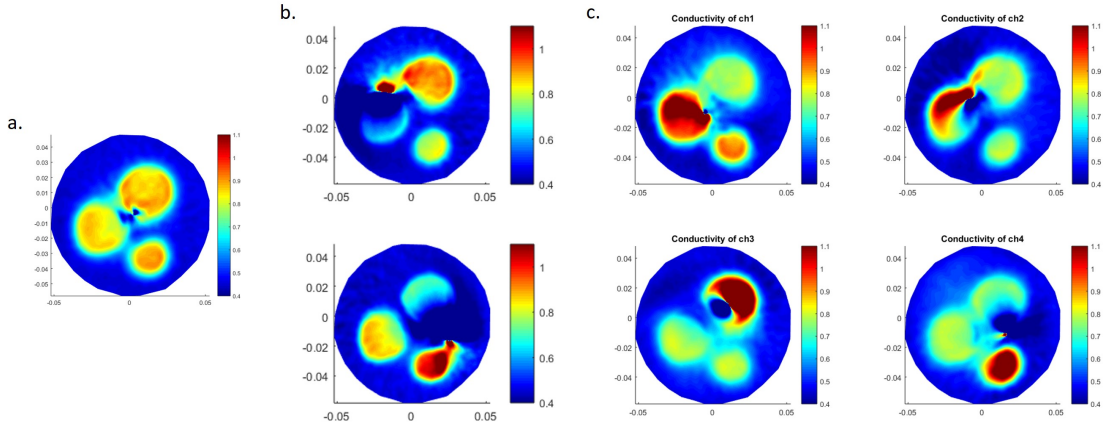

Figure 4.2: cr-MREPT conductivity reconstructions (S/m) for a. Original method, b. Left pad (upper row) and Right pad (below row), c. each channel of the multichannel data

Figure 4.3 gives the cr-MREPT combined reconstructions of padding and multichannel data. LP and RP combination eliminates the LCF artifact. 4 channel data is combined using 2 channel data at a time and the resulting conductivity images are given in Figure 4.3.c. Non-consecutive channel combinations, ch1&ch3 and ch2&ch4, give better accuracy than the consecutive channel combinations. All combinations cleared the conductivity maps from the dips created by the LCF artifact in Figure 4.3.a. In the background region between the anomaly regions, there is an increase in the conductivity values. This is also the case in the individual channel conductivity maps. This erroneous reconstruction is due to the phase distributions used in the solutions as this distributions not only carry the transmit phase information but also the receive phase information that is not a component of the equation. Figure 4.3.d displays the conductivity values for each channel on a profile (profile lines and the expected conductivity maps are given in 3.14) and also the results of the original method

and the padding method are plotted. Similar to the images, profiles also show that non-consecutive channel combinations are better in accuracy, especially ch2&ch4 in this example.

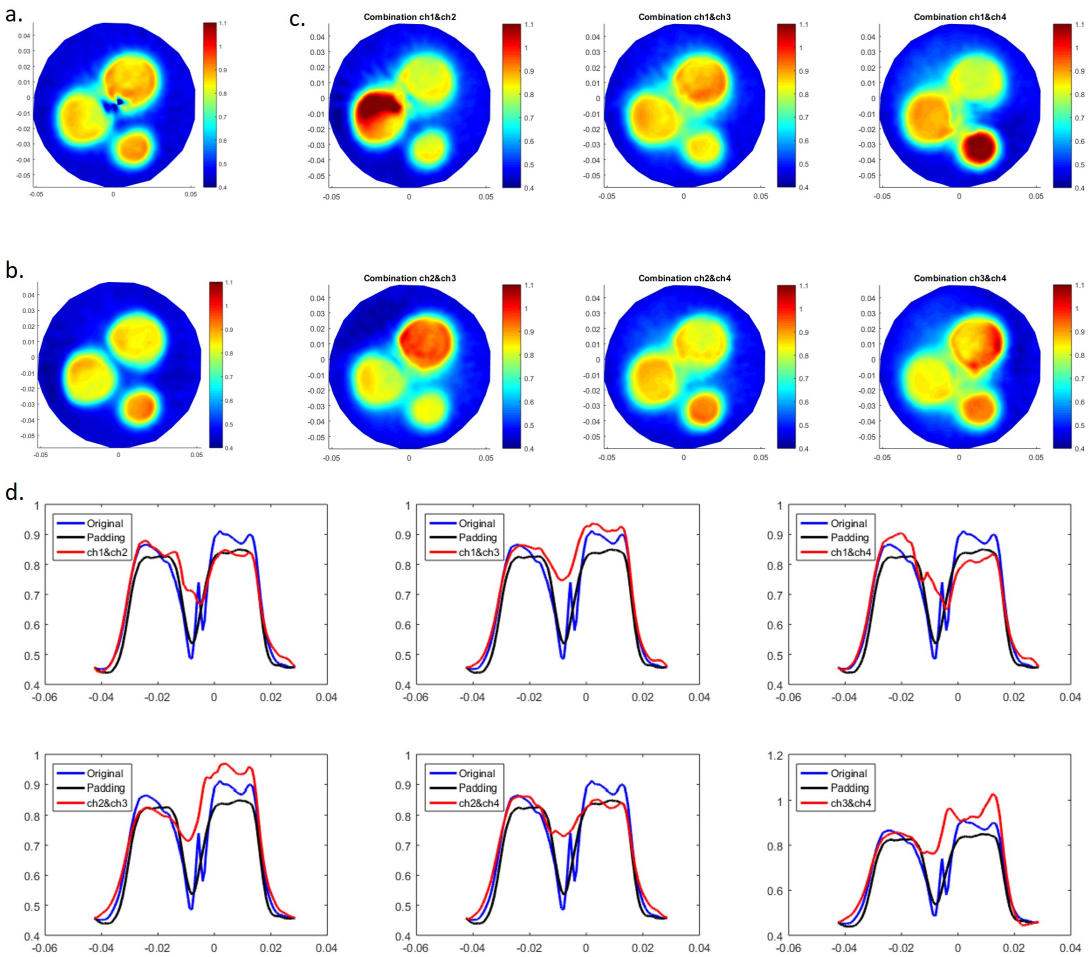

Figure 4.3: cr-MREPT conductivity images (S/m) for: a. Original method, b. LP + RP combination, c. bi-channel combinations of multichannel receive data, d. Conductivity profiles (S/m) for each combination and also for the original and the padding method.

Figure 4.4 displays the combinations of 3 channels at a time. Since every combination has the non-consecutive channels, there are no extreme values with these combinations.

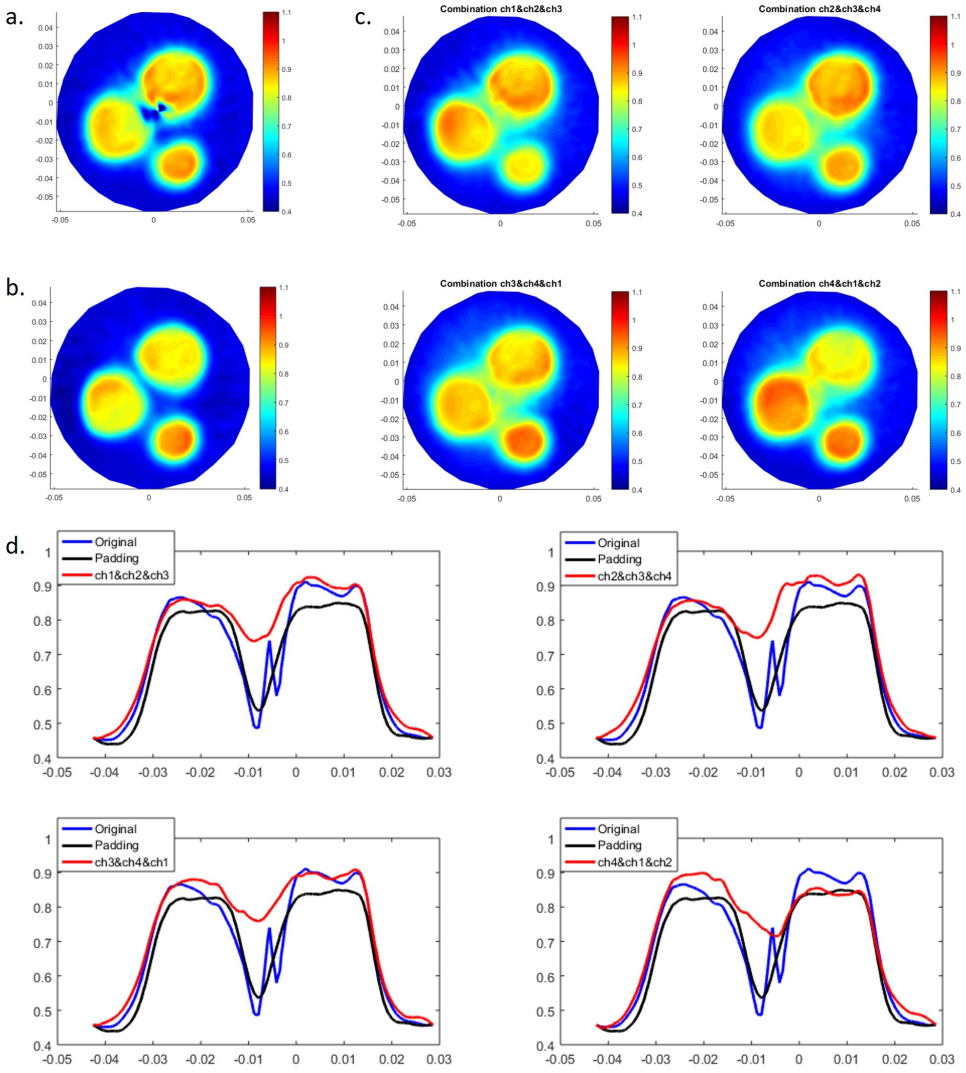

Figure 4.4: cr-MREPT conductivity images (S/m) for: a. Original method, b. LP + RP combination, c. three-channel combinations of multichannel receive data, d. Conductivity profiles (S/m) for each combination and also for the original and the padding method.

Figure 4.5 shows the 4-channel combined conductivity reconstruction. All anomaly regions have similar conductivity values as expected and the background away from the anomalies gives the expected conductivity values as well. On the other hand, original method and the padding method reconstructions produce conductivity values that are different than each other in the anomaly regions. Padding method reconstruction has less fluctuations which is also as expected.

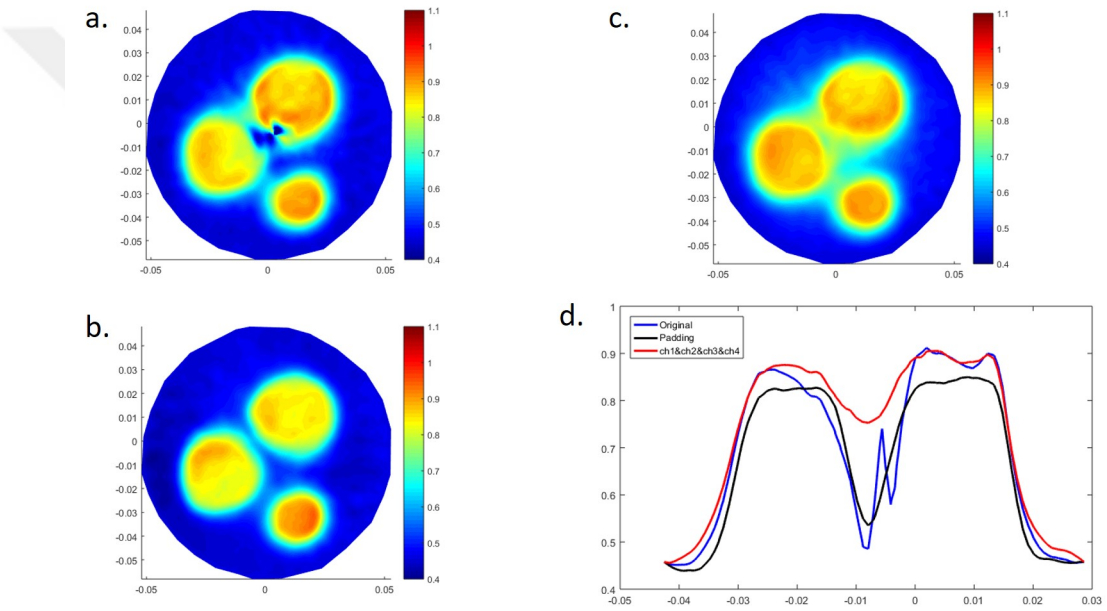

Figure 4.5: cr-MREPT conductivity images (S/m) for: a. Original method, b. LP + RP combination, c. four-channel combination of multichannel receive data, d. Conductivity profiles (S/m) for our-channel combination and also for the original and the padding method.

Figure 4.6 displays the results of another phantom (expected conductivity map is given in 3.14). A non-consecutive two-channel combination and a four-channel combination of multichannel data is given with the conductivity reconstructions of the original method an the padding method (where Entekno $BaTiO_3$ pad is used again and the LP+RP cases are combined). Padding result gives the best accuracy at the background. Anomaly regions all should have the same conductivity reconstruction and two-channel combination succeeds that. All combinations eliminate the LCF artifact. Although, it is known that channel combination uses the wrong phase distribution, the results are not much different than the original method result and besides it does not contain the LCF artifact.

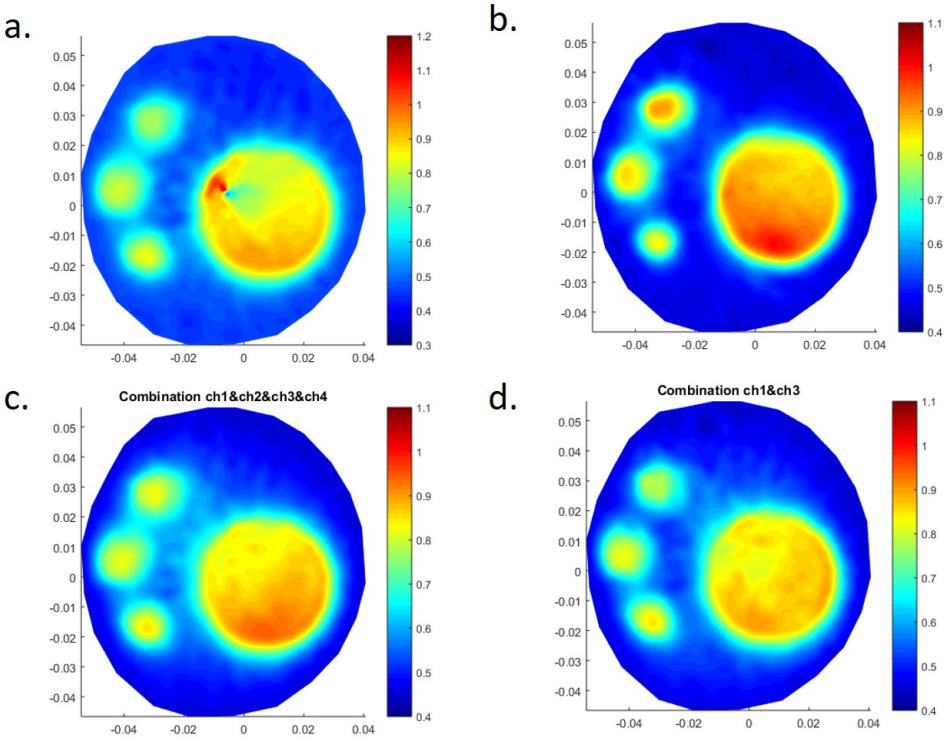

Figure 4.6: cr-MREPT conductivity images (S/m) for: a. Original method, b. LP + RP combination, c. four-channel combination of multichannel receive data, d. Conductivity profiles (S/m) for four-channel combination and also for the original and the padding method.

4.3 Discussion

While cr-MREPT suffers from LCF artifact and the padding method which removes LCF artifact requires additional acquisitions, the proposed method is advantageous in both aspects, namely reduction of LCF artifact and not requiring additional acquisition. However, padding method gives numerically closer results to the expected values than the proposed method in general. First reason is that TPA does not hold in individual channel data sets and the second reason is the fact that the LCF regions are not sufficiently far from each other, on contrast to padding method. Although the proposed method lacks accuracy, it is time-saving and artifact-free, which may make it a good choice in practical use especially for portraying contrast variations in conductivity.

Chapter 5

Conclusion

As a potential diagnostic tool and being essential for local specific absorption rate calculation, MR based EPT is an attractive research area. Moreover, MREPT has several benefits compared to other electrical property imaging algorithms. It does not require external current flow through electrodes and has high spatial resolution. Although conventional MREPT algorithm has limitations as the boundary artifact issue and the noise prone behavior, several algorithms [24–26] have been proposed to overcome these problems of MREPT. Handling the boundary artifact and the noisy nature of the conventional method, there is nevertheless the LCF artifact issue. This problem is named differently by other investigators such as "global bias" in g-EPT [27], but the behavior of the artifact is the same. In convection-reaction MREPT, the artifact occurs at the region of low convective field region. In this thesis, two methods are proposed to get rid of the LCF artifact.

Padding technique is one of the proposed methods to improve the cr-MREPT method. Both simulation and experimental results indicate that the LCF artifact is corrected in conductivity images. It also should be stated that the accuracy of the conductivity values are improved. Furthermore, the studied behavior of dielectric and conductive pads onto the measured magnetic field may also be useful for B_1 shimming studies.

The amount of the LCF shift is very important in the aspect of obtaining non-overlapping LCF regions, yet too much shift results in unexpected errors in the images. When the H_Z field (component of the magnetic field in the z-direction), that is neglected in the previous studies [6], was analyzed in the simulation environment, it is observed that when no pad is used the spatial derivatives of H_Z are negligible with respect to the H^+ terms. However, when a dielectric and/or conductive pad is introduced near the object, the spatial derivatives of H_Z become more pronounced and the values get closer to the H^+ terms as the EPs of the pad is increased. In simulation studies, when the H_Z term in Eq. (2.2.1) is added to the computation, the error in the conductivity reconstructions are corrected (see Figure 3.9). Since there is no method to gather H_Z field information experimentally, it is not possible to correct these errors. One may want to use relatively lower EP values for their pad, to avoid these erroneous results. Alternatively, one may use higher EP valued pads but keep the thickness minimum to decrease the total effect.

An important drawback of the padding method is the time it demands for data acquisition. While only one excitation is enough for the conventional cr-MREPT method or conventional MREPT methods, padding technique requires at least double the time or even more (if additional with or without pad positions are desired) than the conventional methods require. In general, left pad and right pad combination gives the best result since the distance between the LCF regions is likely to be further with this pair and two consecutive excitations are enough for the method. Yet, the total required time may exceed the comfortable level in a clinical application.

The second method that has been proposed utilizes channel sensitivities as a means to shift the LCF region and combining the different channel data results in LCF-free conductivity images. This method get ahead with the shorter acquisition time. The multichannel receive technique is able to obtain the necessary data to get rid of the LCF artifact with only one excitation. Therefore, making it superior to the conventional cr-MREPT method as there is no LCF artifact and superior to padding technique as it requires at least half the acquisition time.

Transceive phase approximation, which is used in all the compared methods, fails to validate for a quadrature Birdcage transmit coil and Phased-array receive coil pair. Therefore the phase utilized for the latter method is not the true transmit phase but also contains the receive phase. As mentioned in the previous chapter, since the transmit phase is the same for all channel data, obtaining the true transmit phase would not give us any advantages. On the other hand, Gurler has proposed using receive field for both the magnitude and the phase and developed a $B1^-$ based cr-MREPT method [51, 52]. This method required additional acquisition that uses TPA first to find the transmit phase and then compute receive field accordingly. Along with the extra acquisition, the resulting conductivity images have more pronounced LCF artifacts and combination of different channel data is not very successful at eliminating the LCF artifact.

TPA may not be valid also for QBC transmit and QBC receive system. If the object of interest is not symmetric, then TPA does not perfectly hold. Furthermore, the phase that amplifiers add is a constant phase and it does not affect the solution since the phase offset is not important in cr-MREPT equation. Using bSSFP sequence, the phase is minimally affected by B_0 field and T_2 of the object, whereas there are some methods to get rid of them [53, 54]. bSSFP does not get affected by eddy current effects unlike spin-echo based methods. Therefore, by using bSSFP, we get minimally affected by the sequence based problems.

One future work may be comprised of using shorter pulse sequence for B_1 magnitude and phase acquisition. Although phase-based MREPT algorithms are preferred for their short pulse sequence sufficiency, they lack the information embedded in B_1^+ magnitude and therefore they are not accurate enough for quantitative imaging. Accelerating the process of obtaining B_1^+, padding method may be a good candidate for clinical use due to both more comfortable imaging time and sharper images, which can be reconstructed with the higher SNR data.

Regularization methods have been proposed by several investigators in order to reduce noise effects and/or algorithm-caused spurious oscillations [35, 55]. Also as mentioned in the introduction, artificial diffusion, which is another way of

regularization, is proposed for reduction of the LCF artifact [33,34]. In this work we have not utilized any regularization method because we wanted to concentrate on the performance and limitations of the padding and the multichannel receive technique. Future work may cover combined use of regularization and the proposed methods as well as the comparison of the two approaches.

Bibliography

[1] C. L. R. J. W. Joines, Y. Zhang, "The measured electrical properties of normal and malignant human tissues from 50 to 900 MHz," *Med Phys.*, vol. 21, no. 4, pp. 547–550, 1994.

[2] A. J. Surowiec, S. S. Stuchly, J. R. Barr, and A. Swarup, "Dielectric Properties of Breast Carcinoma and the Surrounding Tissues," *IEEE Transactions on Biomedical Engineering*, vol. 35, no. 4, pp. 257–263, 1988.

[3] P. F. F Salinas, J Lancaster, "3D modeling of the total electric field induced by transcranial magnetic stimulation using the boundary element method," *Physics in Medicine and Biology*, vol. 54, pp. 3631–3647, 2009.

[4] G. S. E Balidemaj, H Kok, "Hyperthermia treatment planning for cervical cancer patients based on electrical conductivity tissue properties acquired in vivo with EPT at 3 T MRI," *International Journal of Hyperthermia*, vol. 32, pp. 558–568, 2016.

[5] H. K. O Kwon, M Chauhan, "Fast conductivity imaging in magnetic resonance electrical impedance tomography (MREIT) for RF ablation monitoring," *International Journal of Hyperthermia*, vol. 30, pp. 447–455, 2014.

[6] U. Katscher *et al.*, "Determination of Electric Conductivity and Local SAR Via B_1 Mapping," *IEEE Transactions on Medical Imaging*, vol. 28, no. 9, pp. 1365–1374, 2009.

[7] D. C. Barber and B. H. Brown, "Applied potential tomography," *Journal of Physics E: Scientic Instruments*, vol. 17, p. 723, 1984.

[8] D. I. M. Cheney and J. C. Newell, "Electrical impedance tomography," *SIAM Review*, vol. 41, pp. 85–101, 1999.

[9] J. C. N. P. M. Edic, G. J. Saulnier and D. Isaacson, "A real-time electrical impedance tomograph," *IEEE Transactions on Biomedical Engineering*, vol. 42, pp. 849–859, 1995.

[10] D. I. D. G. G. L. F. Fuks, M. Cheney and J. C. Newell, "Detection and imaging of electric conductivity and permittivity at low frequency," *IEEE Transactions on Biomedical Engineering*, vol. 38, pp. 1106–1110, 1991.

[11] Y. Z. I. N. G. Gencer and S. J. Williamson, "Electrical impedance tomography: induced-current imaging achieved with a multiple coil system," *IEEE Transactions on Biomedical Engineering*, vol. 43, pp. 139–149, 1996.

[12] H. Griffiths, "Magnetic induction tomography," *Measurement Science and Technology*, vol. 12, p. 1126, 2001.

[13] Y. Z. Ider and O. Birgul, "Use of the magnetic field generated by the internal distribution of injected currents for electrical impedance tomography (MREIT)," *ELEKTRIK*, vol. 6, pp. 215–225, 1998.

[14] Y. Z. Ider and S. Onart, "Algebraic reconstruction for 3D magnetic resonance electrical impedance tomography (MREIT) using one component of magnetic flux density," *Physiological Measurement*, vol. 25, p. 281, 2004.

[15] E. J. W. J. K. Seo, J.-R. Yoon and O. Kwon, "Reconstruction of conductivity and current density images using only one component of magnetic field measurements," *IEEE Transactions on Biomedical Engineering*, vol. 50, pp. 1121–1124, 2003.

[16] E. J. W. J. K. Seo and O. Kwon, "Magnetic resonance electrical impedance tomography (MREIT): conductivity and current density imaging," *Journal of Physics: Conference Series*, vol. 12, p. 140, 2005.

[17] E. J. W. J. K. Seo, "Magnetic resonance electrical impedance tomography (MREIT)," *SIAM Review*, vol. 53, pp. 40–68, 2011.

[18] J.-R. Y. O. Kwon, E. J. Woo and J. K. Seo, "Magnetic resonance electrical impedance tomography (MREIT): simulation study of j-substitution algorithm," *IEEE Transactions on Biomedical Engineering*, vol. 49, pp. 160–167, 2002.

[19] C. P. H. S. Nam and O. I. Kwon, "Non-iterative conductivity reconstruction algorithm using projected current density in MREIT," *Physics in Medicine and Biology*, vol. 53, p. 23, 2008.

[20] R. L. A. G. C. Scott, M. L. G. Joy and R. M. Henkelman, "Measurement of nonuniform current density by magnetic resonance," *IEEE Transactions on Medical Imaging*, vol. 10, pp. 362–374, 1991.

[21] J. K. S. E. J. Woo, "Magnetic resonance electrical impedance tomography (MREIT) for high-resolution conductivity imaging," *Physiological Measurement*, vol. 29, p. 29, 2008.

[22] E. N. D. W. E Haacke, L Petropoulos, "Extraction of conductivity and permittivity using magnetic resonance imaging," *Physics in Medicine and Biology*, vol. 36, pp. 723–734, 1991.

[23] H. Wen, "Extraction of conductivity and permittivity using magnetic resonance imaging," in *Proceedings of SPIE 5030, Medical Imaging: Physics of Medical Imaging 2003*, (San Diego, CA, USA), 2003.

[24] S. S. P. V. d. M. B. H. J Liu, X Zhang, "Gradient-based electrical properties tomography (gEPT): A robust method for mapping electrical properties of biological tissues in vivo using magnetic resonance imaging," *Magnetic Resonance in Medicine*, vol. 74, pp. 634–646, 2014.

[25] E. Balidemaj *et al.*, "CSI-EPT: A Contrast Source Inversion Approach for Improved MRI-Based Electric Properties Tomography," *Ieee Transactions on Medical Imaging*, vol. 44, no. 9, pp. 1788–1796, 2015.

[26] F. S. Hafalir, O. F. Oran, N. Gurler, and Y. Z. Ider, "Convection-Reaction Equation Based Magnetic Resonance Electrical Properties Tomography (cr-MREPT)," *IEEE Transactions on Medical Imaging*, vol. 33, no. 3, p. 456–466, 2014.

[27] J. Liu, Y. Wang, U. Katscher, and B. He, "Electrical Properties Tomography Based on B_1 Maps in MRI: Principles, Applications and Challenges," *IEEE Transactions on Biomedical Engineering*, 2017. 10.1109/TBME.2017.2725140.

[28] A. W. R Schmidt, "A new approach for electrical properties estimation using a global integral equation and improvements using high permittivity materials," *Journal of Magnetic Resonance*, vol. 262, pp. 8–14, 2014.

[29] G. Ariturk and Y. Z. Ider, "Optimal multichannel transmission for improved cr-MREPT," *Physics in Medicine and Biology*, vol. 63, no. 4, 2018.

[30] N. Gurler and Y. Z. Ider, "Gradient- Based Electrical Conductivity Imaging Using MR Phase," *Magnetic Resonance in Medicine*, vol. 77, pp. 137–150, 2016.

[31] A. L. H. M. W. Van Lier *et al.*, "B_1^+ Phase Mapping at 7T and its Application for In Vivo Electrical Conductivity Mapping," *Magnetic Resonance in Medicine*, vol. 67, pp. 552–561, 2012.

[32] T. Voigt, U. Katscher, and O. Doessel, "Quantitative Conductivity and Permittivity Imaging of the Human Brain Using Electric Properties Tomography," *Magnetic Resonance in Medicine*, p. 456–466, 2011.

[33] C. Li, W. Yu, and S. Y. Huang, "An MR-Based Viscosity-Type Regularization Method for Electrical Property Tomography," *Tomography*, vol. 25, no. 1, pp. 50–59, 2017.

[34] C. B. YZ Ider, "Spatial resolution of Full cr-MREPT: 2D and 3D evaluation," in *Proceedings of the 26th Annual meeting of ISMRM*, (Paris, France), 2018.

[35] K. M. Ropella and D. C. Noll, "A Regularized, Model-Based Approach to Phase-Based Conductivity Mapping Using MRI," *Magnetic Resonance in Medicine*, vol. 78, pp. 2011–2021, 2016.

[36] G. Yildiz, G. Ariturk, and Y. Z. Ider, "Use of Padding to Eliminate Low Convective Field Artifact in Conductivity Maps Obtained by cr-MREPT,"

in *Proceedings of the 25th Annual meeting of ISMRM*, (Honolulu, HI, USA), 2017.

[37] C. C. C. W. M. S. Q Yang, J Wang, " Reducing SAR and enhancing cerebral signal-to-noise ratio with high permittivity padding at 3 T," *Magnetic Resonance in Medicine*, vol. 65, pp. 358–362, 2010.

[38] M. K. Q Yang, Z Herse, "Enhancement of RF field by high dielectric constant pad at 3T: cervical spine imaging," in *Proceedings of the 19th Annual meeting of ISMRM*, (Montreal, Canada), 2011.

[39] W. H. G. K. L. S. R. L. B. K. M Schmitt, T Feiweier, "Improved uniformity of RF-distribution in clinical whole body imaging at 3T by means of dielectric pads," in *Proceedings of the 12th Annual meeting of ISMRM*, (Kyoto, Japan), 2004.

[40] A. W. K Haines, N Smith, "New high dielectric constant materials for tailoring the B 1 + distribution at high magnetic fields," *Journal of Magnetic Resonance*, vol. 203, pp. 323–327, 2010.

[41] D. I. Hoult, "The principle of reciprocity in signal strength calculations, a mathematical guide," *Concepts in Magnetic Resonance*, vol. 12, pp. 173–187, 2000.

[42] P. W. R Stollberger, "Imaging of the active B1 field in vivo," *Magnetic Resonance in Medicine*, vol. 35, pp. 246–251, 1996.

[43] I. H. L. I. Sacolick, F. Wiesinger and M. W. Vogel, "Imaging of the active B1 field in vivo," vol. 35.

[44] V. Yarnykh, "Actual flip-angle imaging in the pulsed steady state: A method for rapid three-dimensional mapping of the transmitted radiofrequency"," *Magnetic Resonance in Medicine*, vol. 57, pp. 192–201, 2007.

[45] T. V. J. J. W. L. P. R. L. U. K. Astrid L H M W Van Lier, A. Raaijmakers and C. A. T. van den Berg, "Electrical properties tomography in the human brain at 1.5, 3, and 7T: A comparison study," *Magnetic Resonance in Medicine*, vol. 71,, pp. 354–363, 2014.

[46] G. Y. YZ Ider, G Ariturk, "Spatial and Contrast Resolution of Phase Based MREPT," in *Proceedings of the 25th Annual meeting of ISMRM*, (Honolulu, HA, USA), 2017.

[47] N. Gurler and Y. Z. Ider, "Numerical Methods and Software Tools for Simulation, Design, and Resonant Mode Analysis of Radio Frequency Birdcage Coils Used in MRI," *Concepts in Magnetic Resonance*, vol. 45, no. 1, pp. 13–32, 2015.

[48] E. Iwase, "Electrıcal Conductıvıtıes Of The Salt Solutıons Contaınıng Agar," *Bulletin of the Chemical Society of Japan*, vol. 2, pp. 61–65, 1927.

[49] N. T. F Meskine, M Mezouar, " A Rigid Image Registration Based on the Nonsubsampled Contourlet Transform and Genetic Algorithms," *Sensors*, vol. 10, pp. 8553–8571, 2010.

[50] L. K. FA FernandezA, "Improved uniformity of RF-distribution in clinical whole body imaging at 3T by means of dielectric pads," in *Proceedings of IEEE 15th International Conference on Microwave, Radar and Wireless Communications*, (Warsaw, Poland), 2004.

[51] O. O. N Gurler and Y. Ider, "cr-MREPT using multichannel receive coil," in *Proceedings of the 22th Annual meeting of ISMRM*, (Milan, Italy), 2014.

[52] N. Gurler, O. F. Oran, and Y. Z. Ider, "Combination of Multichannel Receive Data For Local Cr-MREPT," in *Proceedings of the 23th Annual meeting of ISMRM*, (Toronto, Ontario, Canada), 2015.

[53] t. . S Ozdemir, YZ Ider

[54] C. A. v. d. B. Y. S. M. B. J. J. L. L. J. S. H. C. Soraya Gavazzi, Stefano Mandija and A. L. van Lier, "Sequences for transceive phase mapping: a comparison study and application to conductivity imaging," in *Proceedings of the 26th Annual meeting of ISMRM*, (Paris, France), 2018.

[55] B. H. Y Wang, P Van de Moortele, "CONtrast Conformed Electrical Properties Tomography (CONCEPT) based on Multi-channel

Transmission," in *Proceedings of the 25th Annual meeting of ISMRM*, (Honolulu, HI, USA), 2017.

Appendix A

Solution of cr-MREPT Equation

To solve cr-MREPT equation in (2.10), numerical methods are needed to be used. The solution is done on triangular mesh with N_p nodes and N_t triangles. Since 2 dimensional solution is computed, only 1 slice is used. First, this linear equation is discretized as follows:

$$\boldsymbol{C}\boldsymbol{u} + \boldsymbol{R}\boldsymbol{u} = \boldsymbol{v} \tag{A.1}$$

where, $\boldsymbol{C}\boldsymbol{u}$ term corresponds to the convection term, $F \cdot \nabla \boldsymbol{u}$, the $\boldsymbol{R}u$ term corresponds to a part of the reaction term, $\nabla^2 H^+ \boldsymbol{u}$, and the $\boldsymbol{v}$ corresponds to the rest of the reaction term without $\boldsymbol{u}$ component, $i\omega\mu_0 H^+$. $\boldsymbol{u}$ vector consists of the impedance values at the nodes and its size is $N_p \times 1$. $\boldsymbol{C}$ and $\boldsymbol{R}$ matrices contain equations for each triangle, and therefore their size is $N_t \times N_p$. $\boldsymbol{v}$ vector is known for each node and is interpolated to triangle centers such that the matrix sizes match each other. $\boldsymbol{v}$ has the size of $N_t \times 1$. It is assumed that the impedance values on the boundaries are known ($\epsilon_r = 80$ and $\sigma = 0.5$ S/m). The matrices are partitioned to separate the known and unknown $\boldsymbol{u}$ values. $\boldsymbol{u}$ vector can be thought as $\boldsymbol{u} = \begin{bmatrix} \boldsymbol{u}_1 \\ \boldsymbol{u}_2 \end{bmatrix}$, where $\boldsymbol{u}_1$ corresponds to the known admittance values at the boundaries and u_2 corresponds to the unknown impedance values. Then the

whole equation can be partitioned as follows:

$$\begin{aligned}
([\boldsymbol{C}_1|\boldsymbol{C}_2] + [\boldsymbol{R}_1|\boldsymbol{R}_2]) \begin{bmatrix} \boldsymbol{u}_1 \\ \boldsymbol{u}_2 \end{bmatrix} &= \boldsymbol{v} \\
(\boldsymbol{C}_1\boldsymbol{u}_1 + \boldsymbol{C}_2\boldsymbol{u}_2 + \boldsymbol{R}_1\boldsymbol{u}_1 + \boldsymbol{R}_2\boldsymbol{u}_2) &= \boldsymbol{v} \\
(\boldsymbol{C}_2 + \boldsymbol{R}_2)\boldsymbol{u}_2 &= \boldsymbol{v} - (\boldsymbol{C}_1 + \boldsymbol{R}_1)\boldsymbol{u}_1 \\
\boldsymbol{A}\boldsymbol{u}_2 &= \boldsymbol{b}
\end{aligned} \tag{A.2}$$

where $\boldsymbol{A} = \boldsymbol{C}_2 + \boldsymbol{R}_2$ and $\boldsymbol{b} = \boldsymbol{v} - (\boldsymbol{C}_1 + \boldsymbol{R}_1)\boldsymbol{u}_1$. Finally, $\boldsymbol{u}_2 = \boldsymbol{A}^{-1}\boldsymbol{b}$ can be solved directly if $\boldsymbol{A}$ matrix is a square matrix. However, $\boldsymbol{A}$ is not a square matrix and equation number is greater than the unknown number such that "least squares" approach is used while obtaining the inverse. This provides some kind of regularization.

A.1 Data Combination

When using double-excitation or multichannel reception, multiple data are needed to be combined. This combination is not performed on conductivity images but on the linear equations. For example, in the padding method, one may want to combine two data, then both need to follow the previous steps. At the end, there will be two equations: $\boldsymbol{A}_1\boldsymbol{u} = \boldsymbol{b}_1$ and $\boldsymbol{A}_2\boldsymbol{u} = \boldsymbol{b}_2$, in which $\boldsymbol{u}$ vector, the unknown, should be the same but $\boldsymbol{A}$ matrices and $\boldsymbol{b}$ vectors should differ such that the conductivity image doesn't have the LCF artifact. These two data are combined as follows:

$$\begin{bmatrix} \boldsymbol{A}_1 \\ \boldsymbol{A}_2 \end{bmatrix} \boldsymbol{u} = \begin{bmatrix} \boldsymbol{b}_1 \\ \boldsymbol{b}_2 \end{bmatrix} \tag{A.3}$$

Then, the $\boldsymbol{u}$ vector is found by

$$\boldsymbol{u} = \begin{bmatrix} \boldsymbol{A}_1 \\ \boldsymbol{A}_2 \end{bmatrix}^{-1} \begin{bmatrix} \boldsymbol{b}_1 \\ \boldsymbol{b}_2 \end{bmatrix} \tag{A.4}$$

From there, the combined conductivity vector can be found with the following formula: $\boldsymbol{\sigma} = \text{Real}(\boldsymbol{1/u})$.